An Endocytic Capture Model for Skeletal Muscle T-tubule Formation

Thomas E Hall[1]*, Nick Martel[1], Nicholas Ariotti[1], Zherui Xiong[1], Harriet P Lo[1], Charles Ferguson[1], James Rae[1], Ye-Wheen Lim[1], Robert G Parton[1,2]*

[1]Institute for Molecular Bioscience, University of Queensland, Brisbane, Queensland 4072, Australia.

[2]Centre for Microscopy and Microanalysis, University of Queensland, Brisbane, Queensland 4072, Australia.

*Authors for correspondence:

Robert G Parton and Thomas E. Hall

Institute for Molecular Bioscience,

University of Queensland,

Queensland 4072,

Brisbane, Australia

E-mail: r.parton@imb.uq.edu.au or thomas.hall@imb.uq.edu.au

Tel: (61) 7 3346 2032

Mobile: 0421 059 424

Fax: (61) 7 33462339

Abstract

The skeletal muscle T-tubule is a specialized membrane domain essential for coordinated muscle contraction that shows dysmorphology in a number of genetically inherited muscle diseases. However, in the absence of genetically tractable systems the mechanisms involved in T-tubule formation are unknown. Here, we have used the optically transparent and genetically tractable zebrafish system to probe T-tubule development *in vivo*. By combining live imaging with three-dimensional electron microscopy we derived a four-dimensional quantitative model for T-tubule formation. To elucidate the mechanisms involved in T-tubule formation *in vivo* we developed a quantitative screen for proteins that associate with and modulate early T-tubule formation including an overexpression screen of the entire zebrafish Rab protein family. We propose a new endocytic capture model involving i) formation of dynamic endocytic tubules at transient nucleation sites on the sarcolemma ii) stabilization by myofibrils/sarcoplasmic reticulum and iii) delivery of membrane from the recycling endosome and Golgi complex.

Keywords

T-tubule, zebrafish, skeletal, muscle, imaging, Rab, endocytosis

The transverse tubule (T-tubule) system of skeletal muscle is an extensive membrane domain that allows action potentials from innervating neurons to reach the depths of muscle fibres thereby triggering calcium release in a synchronized fashion. The T-tubule system is a vital component of the skeletal muscle, frequently disrupted in muscle disease. This is exemplified by aberrant T-tubules and mutations in key T-tubule components in many human myopathies[1-6]. An understanding of the biogenesis of this enigmatic organelle is necessary for further insight into these diseases, however progress has been compromised by the absence of adequate experimental models.

The T-tubule system develops within a defined, but extended period, in mammalian systems. In the mouse, the T-tubules are first observed as longitudinal elements at E16[7] which gradually become organized into transverse elements from around birth to post-natal day 10[8]. The mature T-tubule system is an elaborate system of surface-connected tubules permeating the entirety of the muscle fibre, and occupying a volume greater than that of the sarcolemma from which is it is thought to be derived[9]. The mature T-tubule system has a protein and lipid composition which is distinct from the sarcolemma, and an extremely precise organization and morphology which includes linear elements and triad junctions at specific points, making contact with the sarcoplasmic reticulum. No cell culture systems faithfully reproduce the development of the highly organized T-tubule system characteristic of vertebrate muscle, and a tractable vertebrate animal model has been lacking until now.

Here, we establish the first *in vivo* model to follow formation of T-tubules in real time. We combine live confocal imaging with state-of-the-art electron microscopic approaches, genome editing and quantitative overexpression screening to define the membrane pathways and molecular processes orchestrating T-tubule development. We derive a new model for T-tubule

formation involving the co-option of existing endocytic pathways and spatially-restricted tubule capture to generate the organized T-tubule system.

Results

Development of an *in vivo* system for real-time visualization of T-tubule development

In order to provide robust visualization of the developing T-tubule system, we first tested several transgenic markers and vital dyes for co-labeling with the T-tubule specific protein Bin1[10] (Fig. 1a-e, Supplementary Fig. 1 a & b). We found that fluorescent proteins tagged with the CaaX domains from either H-ras or K-ras were robustly localized to the T-tubules, as well as to the sarcolemma at 48hpf (Fig. 1a & b). For this reason we obtained an existing transgenic line which strongly and robustly expresses GFP-CaaX in all cells from a ubiquitous promoter to use in our analyses[11]. This general membrane marker allowed us to visualize development of the T-tubule membrane system at an early stage without bias caused by focussing on specific proteins. To investigate the development of the T-system during the transition from nascent myotube to muscle fibre, we imaged transgenic embryos from immediately post-fusion of the fast muscle (16hpf), until 48hpf when the T-tubules were observed to penetrate the cell all the way from the sarcolemma to the midline of the fibre (Fig. 1f, Supplementary Videos 1 and 2). Direct measurements from still images showed that the T-tubules adopted a regular spacing at 1.9µm intervals.

A quantitative model for formation and expansion of the T-tubule system

In order to understand the development of the T-system in a quantitative manner, and to probe more deeply our observations from light microscopy, we turned to electron microscopy. We used a potassium ferricyanide stain on thin transmission electron microscopy (TEM) sections

to specifically label the T-tubules[8] and distinguish them from sarcoplasmic reticulum (SR). Sections taken at 16hpf showed electron dense, transverse oriented tubular membranes associated with the forming Z-lines (arrow Fig. 2a). By contrast, transverse sections taken towards the centre of the sarcomere some distance away from the Z-lines showed association of longitudinal sarcoplasmic reticulum (identifiable by its beaded appearance and lower electron density) with the early myofibrillar material (arrowhead, Fig. 2c). By 48hpf, the myofibrillar bundles, analogous to previously described "nascent myofibrils"[12] developed longitudinal furrows as they increased in diameter consistent with the Goldspink model of myofibrillar splitting during growth[13] (Fig. 2b, d-f). Thin sections and serial blockface scanning electron microscopy with 3D reconstruction showed that these furrows contained SR and, at the level of the Z-line, T-tubules (Fig. 2b, d-j, Supplementary Video 3). Tracing of thin sections taken between 16hpf and 10dpf showed that furrows develop in a spatially predictable manner, such that each contractile filament maintains close proximity to a furrow, and consequently a T-tubule (Fig. 2k). We reasoned that these reiterated spatial relationships would be amenable to mathematical modeling.

To produce a quantitative mathematical model of membrane sequestration into the forming tubules, we required more accurate empirical data from larger numbers of developing muscle fibres than is possible using serial blockface methods. Instead, we assembled large mosaics of tiled TEM micrographs covering entire transverse sections through the trunk musculature at 48hpf, 5dpf and 10dpf. Using custom written image analysis macros we were able to produce masks defining muscle fibres, myofibrils and furrows within a half-section through an entire animal (Fig. 3a-c), and extract morphometric data (Fig. 3d & e, Supplementary Fig. 3a-c).

Using the functions derived from these empirical measurements, and from measurements of somite width (Fig. 3f; a proxy for fibre length) and T-tubule diameter (Fig. 3g), we derived a single equation to predict the total surface area of T-tubule membrane within muscle fibres of specified length and diameter (Supplementary Fig. 3d-g, full details are given in the Methods). With this model we calculated that the T-tubule system (undetectable at 16h), has developed into a complex organelle with a surface area comprising 35% of the total surface area of the cell (2579 : 4817 μm^2; T-system : sarcolemma) by 48hpf (total surface area = T-system surface area + sarcolemma). By 5dpf the relative surface area of the T-tubule domain gradually increases to 40% (4737 : 7092 μm^2) and after 10dpf will eclipse the surface area of the sarcolemma (13695 : 14456 μm^2; 49%). For the largest fibres in adult fish, we applied our model to fibres from a 12 month old male from the zebrafish atlas (http://bio-atlas.psu.edu/zf/view.php?s=220&atlas=18; http://bio-atlas.psu.edu/zf/view.php?s=275&atlas=17), where the largest fibres are approximately 580µm in length and have diameters of up to 40µm. In these fibres, our model predicts that the T-tubule system has approximately 1.5 times of the total surface area of the cell (Fig. 3h & i). The increase in surface area of the two membrane systems during the two early time periods correspond to an average of ~1.03 μm^2 /minute of new membrane addition for the entire 48h-5dpf period and ~2.27 μm^2/minute for the 5dpf to 10dpf period. These results emphasize the magnitude of new membrane synthesis and, necessarily, flow through and delivery from the Golgi complex to allow this membrane expansion. Previous studies have suggested a maximal rate of approximately 2.7μm^2 of membrane per minute for passage through the Golgi complex in rapidly dividing transformed cell lines[14] which would be adequate for the generation of the T-tubule system and for the expansion of the sarcolemma based on our estimates. However, additional membrane synthesis would obviously be required for the generation and expansion of the other crucial membrane systems during this period such as the SR. This implies that

specific cellular machinery must be upregulated at the onset of T-tubule formation, including components required for membrane synthesis, for sorting, and for targeted delivery to specific domains including the T-tubule system during this growth period.

Transverse tubule stability is dependent upon sarcomere formation and integrity

The strict association of the T-tubules with the sarcomeric Z-lines led us to question whether the contractile apparatus was involved in the scaffolding of T-tubules during development. To examine further the relationship of sarcomerogenesis to T-tubule development, we made a transgenic line expressing a red fluorescent protein fused to the lifeact tag[15], which labels F-actin, including sarcomeric actin. Live imaging of fish carrying both red Lifeact and green CaaX transgenes revealed transverse tubules invariably extended inwards towards the midline of the cell while maintaining a perpendicular association with the developing actin-containing myofibrils (Fig. 4a & b, Supplementary Video 4), in agreement with our EM data. Examination of the sarcoplasmic reticulum, marked by another stable transgenic line expressing a red fluorescent protein tagged with an N-terminal calreticulin signal sequence and a C-terminal (KDEL) ER retention sequence, showed that the SR also adopts a regular, Z-line associated arrangement upon sarcomerogenesis (Fig. 4c-d). Titin cap (Supplementary Fig. 4a-b), alpha-actinin (c-d) and junctophilin 1a (e-f) were also spatially associated with T-tubule development, whereas SERCA1, a marker of the non-junctional SR was specifically excluded from the CaaX positive T-domain (g-h). Finally, in order to test directly whether tubule formation is directly dependent upon the sarcomere, we employed a loss of function approach using CRISPR-Cas9[16]. We generated embryos possessing null alleles of slow myosin heavy chain (the only myosin expressed in zebrafish slow muscle at early stages[17]). All slow muscle cells in these embryos showed a reduction in the distance between T-tubules, reflecting a "concertina effect" on the sarcomeres, where the Z-lines became closer together (Fig. 4e, g).

Next, we generated a null allele of titin, the "molecular scaffold" which links myosin filaments to the Z-line[18]. In these mutants, the T-tubules completely lost their transverse structure and instead became a disorganized meshwork (Fig. 4f). TEM images showed unstructured myosin and actin filaments and narrow unstructured electron dense tubules (Fig. 4h-j). We noted however, the stochastic coalescence of junctional SR and electron dense tubule (arrows, Fig. 4i & j). Quantitation of the diameters of SR-associated vs non-SR associated T-tubule in titin mutants showed a 90% increase in average diameter (43.5 vs 22.8µm) in tubules associated with SR, suggesting that tubule morphology is influenced by interactions with SR or thin filament components (Fig. 4k).

Surface connected tubules are stabilised by "endocytic capture" to form transverse orientated tubules

The tight association of the forming T-tubules with the Z-line and junctional SR led us to investigate further the first interactions of the tubules with the forming contractile apparatus. Using live imaging, we observed at the earliest stages, both tubular and vesicular CaaX positive structures beneath the plasma membrane (Fig 5a-c). These tubular structures appeared to then become stabilized into the familiar transverse-orientated tubules regularly spaced at 1.9µm intervals. We next asked whether, during formation, the T-tubules are in fact surface-connected, or whether the nascent tubule begins as an internal compartment which opens to the extracellular milieu later in development. To test this, we performed intramuscular injection of Alexa-647 labelled UTP, which has been used as a low molecular weight fluorescent tracer that is unable to cross an intact plasma membrane[19]. Injection of the tracer into 16, 24 or 48 hpf GFP-CaaX zebrafish resulted in immediate infiltration into the tubules, confirming surface connectivity (Figs. 5d-f). Similarly, uptake of the fluid-phase marker Alexa-647-dextran (10,000MW), also resulted in immediate infiltration into the tubules, whereas uptake into

putative endosomes only occurred after several minutes (Fig. 5g, Supplementary Video 5). Serial blockface scanning electron microscopy and 3D reconstruction of 48hpf fibres at high resolution showed narrower tubular connections between the plasma membrane and the stabilized, sarcomere associated tubules (Fig 5h). In areas where sarcomeres were separated from the plasma membrane by cytoplasm, these connecting tubules frequently looped and formed connections to the sarcolemma some distance from their origin (Supplementary Fig. 5a). Injection of unconjugated horse radish peroxidase into the circulation at 48hpf also resulted in infiltration into the tubules (Supplementary Fig. 5b & c). Taken together with our analyses of *smyhc1* and *titin* mutants, these data suggest that the earliest detectable tubules are surface-connected and are therefore analogous to endocytic tubules. In this model, tubules derived from the sarcolemma would be stabilized when they interact with the contractile apparatus either directly, or through specification of the junctional sarcoplasmic reticulum, a process which we term "endocytic capture".

Molecular composition of the early T-tubules

In order to probe the composition of the early tubules in zebrafish muscle, and to gain insight into their biogenesis, we sought to examine the localization of the zebrafish orthologues of a suite of trafficking and T-tubule associated markers previously defined in mammalian systems (Fig. 6a-j). We developed a set of computational tools which allowed us to perform quantitative analyses of the association of transiently-expressed fluorescently-tagged proteins with the T-tubules in an unbiased fashion with reasonable throughput. Using this pipeline, we were able to calculate localization values for defined domains, in this case T-tubule and sarcolemma (Fig. 6i & j) from large numbers of replicated images using ImageJ (full code is given in Supplementary Macros). We were also able to calculate the extent of T-tubule perturbation, by comparing the amplitude of CaaX intensity along the longitudinal axes of the cells (Fig. 6k-

m). These analyses showed a striking and selective enrichment of a subset of these proteins; Bin1b, Cavin4a and Cavin4b, EHD1a, Cav3, Dynamin2b and CD44b to the area of the Z-line and junctional SR (Fig. 6a-j, Supplementary Fig. 6a-g). Localisation of these factors to this intracellular domain suggested an endocytic tubule formation mechanism with similarities to those described in non-muscle cells[20, 21]. To test a functional role for these proteins, we generated dominant negative forms of these proteins where possible, and compared the amplitude plots of the CaaX marker as a measure of the extent of perturbation (Fig. 6l & m). We found a marked reduction in amplitude with expression of some of the dominant negative forms, in particular, EHD1a-dEH and EHD1b-dEH (Fig. 6d & m, Supplementary Fig. 6a & b). Notably, in the cases of EHD1a and EHD1b, tubule intensity was also increased when the wild-type proteins were expressed. These analyses demonstrate that endocytic protein function is necessary for the normal development of the T-system and suggests a model where formation occurs by co-option of existing endocytic machinery.

Next, we used a set of well-established probes to examine the phosphoinositide composition of the T-tubules, since different membrane compartments have particularly distinct phosphoinositide signatures. T-tubule phosphoinositide composition has not been directly studied *in vivo*, although enrichment of PtdIns(4,5)P_2 on early tubules in C2C12 cells, and a tenfold increase in total phosphoinositides upon differentiation into myotubes have been demonstrated[10]. Of all probes tested, LactC2/PS, had the highest T-tubule signal (Fig. 7a, h) consistent with a previous biochemical study[22]. We also found substantial levels of BTK/PtdIns(3,4,5)P_3 (Fig. 7b, h) and PLC-D/PtdIns(4,5)P_2 (Fig. 7c, h) in early T-tubule membranes. Of the other probes used, ING/ PtdIns(5)P showed a small but significant localization to the tubules (Fig. 7d, h), FAPP1/ PtdIns(4)P was largely confined to the Golgi complex as expected (Fig. 7e), ATG18/ PtdIns(3,5)P_2 labelled an internal compartment

consistent with lysosomes (Fig. 7f) and 2xFYVE^{hrs}/ PtdIns(3)P gave a punctate pattern consistent with early endosomes (Fig. 7g, see also GalT, lamp1 and EEA1, Supplementary Fig. 7a-c, respectively). These data suggest that a defining feature of the early tubules is a distinct lipid composition, which may form a platform on which other proteins are recruited to establish the distinct protein composition.

An overexpression screen of all zebrafish Rab proteins implicates a subset of endosomal Rabs in T-tubule development

In order to identify specific cellular machinery upregulated or deployed during formation of the T-tubule/SR junction, we performed an overexpression screen of the entire zebrafish Rab family. Rab proteins are key regulators of membrane trafficking, controlling almost every step of vesicle trafficking including formation, transport and fusion. Approximately 60 Rab proteins are involved in different aspects of membrane regulation in mammalian cells and the functions of many of these proteins are well described in non-muscle cells. Indeed, Rab protein overexpression has been shown to have specific functional consequences upon specific membrane trafficking processes, presumably by sequestering key regulators[23], a strategy validated in other *in vivo* screening systems[24]. We generated a muscle-specific expression library by cloning each Rab open reading frame behind a muscle specific promoter and a red fluorescent protein tag. Identified Rab proteins were further tested using specific dominant-acting mutants.

Using this systematic quantitative analysis, we found a subset of Rab proteins with specific localization to the T-tubule/SR junction (Fig. 8a-e, i). This included Rab33bb, Rab32b and Rab40b which all showed strong and specific localization to this region (Fig. 8a-c). Closely related paralogues frequently had markedly different profiles confirming the specificity of the

screen (e.g. compare Rab33bb to Rab33ba, Fig. 8i). Rab8b specifically localized to the tubules (ranked 10th) but also frequently produced ectopic "knots" of CaaX-negative tubules extending beyond the leading front of tubule formation (Supplementary Fig. 8b). In this case, overexpression was also associated with a decrease, rather than an increase in T-tubule intensity (Fig. 8i). In contrast, Rab32b, ranked second for localization, resulted in an approximately 80% increase in CaaX intensity, strongly suggestive of positive regulation of T-tubule formation (Fig. 8i). We found that the most perturbing construct was Rab6a (Fig. 8f, i). Rab6b was not localized to the T-tubules consistent with its role in vesicle fission from the Trans–Golgi Network (TGN)[25]. Strikingly, the next most perturbing group of Rab proteins all belong to a subset of endosomal Rabs, including Rab4a, Rab22a, Rab11ba, Rab5c which are all present on early (Rab22a, 5c) or recycling (Rab11ba, 4a, 22a) endosomes[26-29] (Fig. 8h & i, Supplementary Fig. 8a, Rab11ba and Rab5c images not shown). These effects were confirmed using the lipid marker BODIPY-FLC$_5$-Ceramide (Supplementary Figure 8c-h) to avoid confounding effects specific to the Hras CaaX domain (note that this analysis showed that Rab23 caused redistribution of the CaaX signal, rather than a specific effect on the T-tubules themselves [compare Fig. 8g with Supplementary Fig. 8d] and was therefore omitted from further analysis). The specific role of the most perturbing Rab proteins (Rab6a, 11ba, 4a, 22a and 5c) on T-tubule development were confirmed by over-expression of the dominant negative and constitutively active variants (Supplementary Fig. 8i).

An *in vitro* model of T-tubule formation for validation of novel factors in T-tubule development

Our *in vivo* approach allowed identification of novel rab proteins which localise to the triadic compartment of the sarcomere, where the T-tubules form at the interface of the junctional SR and Z-line. In order to probe further the role of these molecules in a systematic manner, and to

validate their triad association, we developed a non-muscle *in vitro* system based on the readily transfectable baby hamster kidney (BHK) cell line. Upon transfection with zebrafish Bin1b, we found that BHK cells form an extensive plasma membrane-connected tubule system which was able to recruit both the CaaX surface marker, and caveolin3, but not the early endosomal marker snx8[30] (Supplementary Fig. 9e-g).

We took the top ten hits for localisation from our *in vivo* screen, and expressed them in this system. Remarkably, six out of the ten candidates (rab13, 8a, 8b, 33bb, 40b, 26; Fig. 9a-g) co-localised to the induced tubules suggesting that, even in the absence of both sarcomere and junctional SR they are able to be recruited to Bin1b-induced membrane tubules. Two factors (rab32b and 37; Supplementary Fig. 9a & b) marked puncta independent from the Bin1b positive tubules, and a further two did not localise to any discernible structure (rab38a and 19; Supplementary Fig. 9c & d). Combined with the *in vivo* screen, we can conclude that a subset of Rabs associate with the developing T-tubule/SR junction, and that the majority of these are recruited to the minimal Bin1 tubule in a model system.

Discussion

In this study, we have defined the molecular mechanisms underpinning vertebrate T-tubule development. Our unique system, utilizing live imaging of transgenic zebrafish embryos, 3-dimensional electron microscopy, mathematical modeling and semi-automated overexpression screening has allowed dissection of T-tubule formation *in vivo*, a process which has been refractory to study for decades. We propose that initial tubule formation, immediately following muscle fibre fusion, utilizes the machinery of endocytosis. The T-tubule system further develops to become an extensive domain permeating the entire cell and eventually

surpasses the sarcolemma in terms of surface area. Mathematical modeling of this process shows that its continuous growth requires rates of membrane synthesis comparable with those of rapidly dividing transformed cell lines. By combining overexpression screening of the entire zebrafish rab protein family with quantitative microscopic analysis we show a role for a Golgi complex small GTPase and a subset of rab proteins specific to the early and recycling endosomes in the expansion of the T-tubule system.

Based on our quantitative 4D analyses, utilizing advanced light and electron microscopy, we put forward a testable model for skeletal muscle T-tubule formation comprising of three stages. Firstly, tubules derived from the sarcolemma nucleate on the inner leaflet of the plasma membrane. These early tubules possess markers of clathrin independent endocytosis, in particular CD44, EHD1[31] and dynamin2[32, 33]. Furthermore, we were able to reciprocally regulate T-tubule integrity when we over-expressed EHD1a or b in wildtype or dominant negative forms confirming that these proteins play a key role in this process. Secondly, these tubules are stabilized by interactions with the sarcomere, either directly or indirectly via the sarcoplasmic reticulum, a process which we have termed 'endocytic capture'. Our three-dimensional electron microscopy revealed that the spatial positioning of the tubules was dependent upon the splitting of myofibrils to form 'furrows' during growth, a phenomenon described over 30 years ago but which has received little attention since[13]. We present evidence that the sarcomere forms the scaffold for the early T-system, since genetic disruption of the sarcomere has a downstream effect on T-tubule morphology. Scaffolding appears to occur independently of the thick filament, since genetic perturbation by deletion of myosin results only in a change in tubule spacing. Genetic perturbation of titin however, results in dysregulation of T-tubule development such that tubules lose completely any ordered orientation. They are narrower, and form only stochastic junctions with SR, where they are also significantly wider in diameter. This raises the intriguing possibility that T-tubule

recruitment might actually be mediated through maturation of SR, and only indirectly by scaffolding from the sarcomere. In differentiating mouse fibres, the junctional SR appears to form absolutely concomitantly with the transversely oriented tubules[8], and non-transverse tubules, such as longitudinal elements, are not associated with SR. Our data also shows that the tubules extending from the sarcomere to the sarcolemma, remain narrow and tortuous, even after the mature architecture is fully developed, raising the possibility that they may be temporally and spatially dynamic, perhaps even remodeling between contraction cycles. Thirdly, because of the prodigious surface area described by our mathematical model, T-tubule development is sensitive to perturbation of trafficking pathways. It appears that vesicles containing fluid phase dextran might "interact" with the forming tubules, and our data shows that perturbation by overexpression of the endosomal rabs rab11ba, 4a, 22a or 5c, results in significant tubule loss, while the integrity of the sarcomere is preserved. Exactly how this directional membrane traffic into growing tubules is achieved is currently unclear, but a recent study using cultured fibroblasts from centronuclear myopathy patients carrying mutations in myotubularin, demonstrated that the myotubularin-dependent conversion of endosomal PI3P into PI4P is necessary for tethering and fusion of exocytic carriers at the plasma membrane[34]. A similar mechanism regulating vesicle fusion at the T-tubule would provide a common axis for the pathobiology of Bin1-, Dynamin2- or myotubularin-related centronuclear myopathies.

This study provides a new paradigm for the formation and stabilization of the T-tubule system during muscle development and establishes a framework in which to probe specific molecular events, such as causative mutations in human disease etiology.

Author Contributions

Conceptualization, T.E.H. and R.G.P.; Methodology, T.E.H., R.G.P, Z.X., N.A., C.F.; Y.L. Validation, T.E.H.; Formal Analysis, T.E.H.; Investigation, T.E.H., N.M., A.X., N.A., J.R. and C.F.; Resources, T.E.H., N.M., H.P.L., Z.X.; Writing, T.E.H.; Visualization, T.E.H.; Supervision T.E.H. and R.G.P.; Project Administration T.E.H. and R.G.P.; Funding Acquisition T.E.H. and R.G.P.

Acknowledgements

We are grateful to Nick Hamilton for advice on image analysis, ImageJ macro programming and equation simplification and Markus Kerr and Alpha Yap for contributing ideas and comments on the manuscript. This work was supported by fellowships and grants from the National Health and Medical Research Council of Australia (to R.G.P., grant numbers 569542 and 1045092; to R.G.P., grant number APP1044041; and to T.E.H. and R.G.P., grant number APP1099251) as well as by the Australian Research Council Centre of Excellence in Convergent Bio-Nano Science and Technology (to R.G.P., grant number CE140100036). Confocal microscopy was performed at the Australian Cancer Research Foundation (ACRF)/Institute for Molecular Bioscience (IMB) Dynamic Imaging Facility for Cancer Biology, established with funding from the ACRF. The authors acknowledge the facilities, and the scientific and technical assistance, of the Australian Microscopy & Microanalysis Research Facility at the Centre for Microscopy and Microanalysis, The University of Queensland, in particular, Robyn Webb, Rick Webb, and Hui Diao for serial blockface and focussed ion beam electron microscopy.

Competing Financial Interests

None declared

Materials and Correspondence

For materials and reagent requests please address correspondence to thomas.hall@imb.uq.edu.au

Figure Legends

Figure 1

A novel *in vivo* system for T-tubule development.

(**a-e**) The CaaX domain from Hras marks both sarcolemma and T-tubule. Markers were screened at 48hpf for T-tubule specificity on a stable transgenic background expressing Bin1b-Citrine from the endogenous locus. (**a**) CaaX domain from Hras (tH). (**b**) CaaX domain from Kras (tK). (**c**) Myristoylation domain from ARF5[35]. (**d**) BODIPY-TR vital dye[36]. (**e**) GPI anchor from zebrafish folate receptor gamma. (**f**) Time course of tubule formation using stable EGFP-CaaX background. See also Supplementary Videos 1 and 2. Scale bars; **a-e**, 10µm, **f**, 50 µm.

Figure 2

Ultrastructural characterization of T-tubule development.

(**a-f**) Transverse orientated transmission electron microscope (TEM) sections showing early T-tubules and sarcoplasmic reticulum. (**a, b**) Transverse sections through the Z line (Z) at 16 and 48hpf. Electron dense, ferricyanide stained tubules are denoted by arrows. (**c, d**) Equivalent transverse sections taken towards the centre of the sarcomere, some distance from the Z-line. Arrowheads denote sarcoplasmic reticulum, which has an unstained lumen and a "beaded" appearance. (**e, f**) Oblique sections at 5 and 10dpf show both ferricyanide stained, electron

dense tubules (arrows) and sarcoplasmic reticulum (arrowheads). M, M-line, Z, Z-line. See also Supplementary Video 3 (**g-i**) Serial blockface electron microscopy and 3D reconstruction shows association of T-tubules with myofibril furrows or "splits" at level of the Z-line (see also Supplementary Video 3). (**j**) Single planes from a focussed ion beam volume enables precise measurements of tubule morphometrics (quantitative data is shown in Fig. 3g). (**k**) Tracing of TEM images illustrates the architecture of myofibril furrows and associated tubules. Red, tubules/furrows; pink, myofibrils; green, sarcolemma. Full masks are shown in Fig. 3a-c. Scale bars; **a-f**, 1µm. **g-h**, 10µm. **j**, 200nm. **k**, 10µm.

Figure 3

A mathematical model of T-tubule development.

(**a-c**) Tracing of tiled TEM montages allows extraction of quantitative data. (**d**) Relationship between fibre cross sectional area and myofibril cross-sectional area. (**e**) Relationship of myofibril cross sectional area to linear furrow distance. (**f**) Somite width during the first 10 days post fertilization. (**g**) Precise measurements from focussed ion beam volumes shows that T-tubules are elliptical (see also Fig. 2j). (**h & i**) Application of the model for sarcolemmal and T-tubule surface area for muscle fibre sizes up to 40µm diameter x 580µm length. This was the maximum measured from a 1 year old adult male. Dotted line shows the intersect of the two planes. Scale bar; **a-c**, 50µm.

Figure 4

Markers of sarcomere formation and organized sarcoplasmic reticulum are associated spatially with forming T-tubules.

(**a, b**) Lifeact (marks actin). See also Supplementary Video 4. (**c, d**) KDEL (marks endoplasmic/sarcoplasmic reticulum). (**e**) *smyhc1*$^{-/-}$ embryos show intact tubules with reduced

but regular spacing in slow muscle fibres. (**f**) *titin*$^{-/-}$ embryos show dysregulated tubule structure. (**g**) Quantification of inter T-tubule distance in fast and slow fibres from *smyhc1*$^{-/-}$ mutant embryos. (**h**) Transverse TEM section showing WT tubules (arrows). (**i, j**) Transverse TEM sections from *titin*$^{-/-}$ mutants showing difference in morphology between tubules associated with sarcoplasmic reticulum (arrows) and tubules not associated with sarcoplasmic reticulum (arrowheads). (**k**) Quantification of sarcoplasmic reticulum associated and non-associated tubules in *titin*$^{-/-}$ mutant embryos. **** $p < 0.0001$. (**a**, **c)** 24hpf; (**b**, **d, f, k**), 48hpf (**e g**, **h**, **i, j**), 72hpf. Scale bars **a-f**, 5µm. **h-j**, 1µm.

Figure 5

Surface connected tubules are stabilised by "endocytic capture"

(**a-c**) Different tubule morphologies by confocal microscopy. (**a**) Longitudinal elements are frequently seen between forming tubules (arrows) and additional elements appear to connect to the sarcolemma (arrowheads). (**b**) Glancing optical sections across the sarcolemma at 16hpf immediately before "stabilized" transverse orientated tubules become visible, show CaaX-positive tubules directly beneath. (**c**) At 48hpf putative surface connected elements (arrows) are frequently seen in glancing optical sections across the sarcolemma. (**d-f**) Intramuscular injection of Alexa-647 conjugated UTP into EGFP-CaaX fish results in immediate infiltration into the developing T-system. (**d)** 16hpf, (**e)** 24hpf, (**f)** 48hpf. (**g**) Timelapse microscopy of 10,000MW-dextran-Alexa-647 injected EGFP-CaaX fish shows immediate infiltration into the tubules, and uptake into intracellular vesicles within 10 mins (see also Supplementary Video 5). (**h**) Serial blockface electron microscopy and 3D reconstruction shows tubules connecting stabilized, sarcomere associated tubules to the sarcolemma. See also Supplementary Fig. 5a. Individual Z planes are shown in **h1-h6**. Scale bars; **a-c**, 5µm. **d-f**, 10µm. **g-h** 5µm.

Figure 6

Molecular composition of the early T-tubules

Images of the top seven markers for T-tubule localization, compared to a non-tubule marker (ARF6). (**a**) Bin1b. (**b**) Cavin4a. (**c**) Cavin4b. (**d**) EHD1a. (**e**) Exoc6. (**f**) Caveolin3. (**g**) Dynamin2b. (**h**) ARF6. Scale bar, 5µm. (**i**) Schematic showing domains used for localization analysis. TT, T-tubule domain; SL, sarcolemma; IT, inter-tubule domain. (**j**) Markers ranked for T-tubule localization. (**k**) Schematic showing the information captured by lateral optical sectioning of T-tubules by confocal microscopy. The average diameter of the T-tubules in the transverse plane was 96nm when measured precisely by electron microscopy. However these structures can appear to be up as large as 380nm in the *xy* plane of confocal microscope images due to light scatter and can increase to 800nm in the *z*-plane. In this schematic, the T-tubules are scaled to a 380nm diameter, and the optical section is scaled to 800nm. (**l**) Schematic showing analysis strategy for assessment of perturbation. A boxed region of interest was placed over an array of eight T-tubules to give the average pixel intensity in the *y* dimension. This method ensured that quantitative assessment of signal was possible even where T-tubules were fragmented or only partially present. For each sample, amplitude was expressed as a percentage of the wildtype (non-expressing) cell from within the same image. (**m**) Comparison of wildtype and dominant negative variants for proteins amenable to such changes. *$p < 0.05$, **$p < 0.01$, ***$p < 0.001$, ****$p < 0.0001$.

Figure 7

Phosphoinositide signature of the developing T-tubules.

(**a**) LactC2 probe for phosphatidylserine (PS). (**b**) BTK probe for PtdIns(3,4,5)P_2. (**c**) PLC-D probe for PtdIns(4,5)P_2. (**d**) ING probe for PtdIns(5)P. (**e**) FAPP1 probe for PtdIns(4)P. (**f**) ATG18 probe for PtdIns (3,5)P_2. (**g**) 2xFYVEhrs probe for PtdIns(3)P. (**h**) Ranked heatmap

comparing average pixel intensity across each domain (T-tubule, sarcolemma and inter-T-tubule domain), for markers of interest and EGFP-CaaX. Six fibres were analyzed per marker. Scale bars, 5µm. *p < 0.05, **p < 0.01, ***p < 0.001, ****p < 0.0001.

Figure 8

An over-expression screen of the entire zebrafish Rab family identifies distinct Rab proteins with T-tubule specific localization, and Rab proteins with the ability to perturb T-tubule formation. (**a-e**) Top five hits for T-tubule localization. (**a**) Rab33bb. (**b**) Rab32b. (**c**) Rab40b. (**d**) Rab13. (**e**) Rab37. (**f-h**) Top three hits for perturbation of fluorescence amplitude. (**f**) Rab6a. (**g**) Rab23. (**h**) Rab4a. (**i**) Ranked heatmap showing specific localization to the T-tubule domain, and the capacity of Rab overexpression to perturb T-tubule formation. Six fibres were analyzed per marker. *p < 0.05, **p < 0.01, ***p < 0.001, ****p < 0.0001. Scale bars, 5µm. See also Supplementary Fig. 8.

Figure 9

An *in vitro* model of T-tubule formation for validation of novel factors in T-tubule development. Tubules are induced in BHK cells by transfection of zebrafish Bin1b, then assessed for colocalization with specific markers. (**a**) Rab13 (**b**) Rab8a, (**c**) Rab8b, (**d**) Rab33bb (**e**) Rab40b (**f**) Rab26 (**g**) summary graphic showing cells that possess tubules with Bin1b only (magenta), marker only (green) and tubules where bin1b colocalizes with the marker (dual color; (see also Supplementary Fig. 9).

Supplementary Figure 1

Myotubularin and Dysferlin mark the early, CaaX-positive T-tubules.

(**a**) Myotubularin. (**b**) Dysferlin. Scale bar, 10µm.

Supplementary Figure 3

A mathematical model for T-tubule formation

(**a-c**) Muscle fibre cellularity profiles at (**a**), 48hpf (**b**) 5dpf (**c**) 10dpf based on directly measured cross-sectional areas (bottom axis). The top axis represents the equivalent diameter of a perfect circle with the same cross-sectional area. (**d**) Schematic of a "model" muscle fibre illustrating the parameters used to calculate T-tubule and sarcolemmal surface area. (**e**) Equation for T-tubule surface area based on the input parameters shown in d. Sections of the equation are colour coded to show source. (**f**) Simplified version of the formula shown in e, with the same input parameters. (**g**) Simplified version of the equations shown in e and f, with the constant parameters *d1*, *d2* and *s* amalgamated, leaving only *L* and *D*. A third version of the equation where diameter (*D*) is replaced by cross sectional area is also given in the Methods.

Supplementary Figure 4

Markers of sarcomere formation and organized sarcoplasmic reticulum are associated spatially with forming T-tubules.

(**a, b**) Titin cap (TCAP/telethonin). (**c, d**) Alpha-actinin2 (actn2). (**e, f**) Junctophilin 1a (Jph1a). (**g-h**) sarcoplasmic/endoplasmic reticulum calcium ATPase 1 (SERCA1). (**a**, **c**, **e**, **g)** 24hpf; (**b**, **d**, **f**, **h)**, 48hpf. Scale bar, 5µm.

Supplementary Figure 5

Surface connected tubules are stabilised by "endocytic capture"

(**a**) Serial blockface electron microscopy and 3D reconstruction shows tubules connecting stabilized, sarcomere associated tubules to the sarcolemma. Where the sarcomere is some distance from the sarcolemma, connecting tubules are often unstructured and looping (arrows).

Individual Z planes are shown in **a1-a8**. (**b**, **c**) Injection of unconjugated horse radish peroxidase into the circulation at 48hpf results in infiltration into the T-tubules after 45 min. Scale bars, 5µm.

Supplementary Figure 6

Selected endocytic markers localize to the T-tubules and dominant negative forms perturb T-tubule formation.

(**a**) EHD1b (**b**) EHD1b-dEH (**c**) Dnm2a (**d**) Dnm2a-DN (**e**) Dnm2b-DN (compare with Fig. 6g) (**f**) EHD1a-dEH (compare with Fig. 6d). (**g**) ARF6-DN (compare with Fig. 6h). Scale bar, 5µm.

Supplementary Figure 7

Non-phosphoinositide binding markers of intracellular domains.

(**a)** 1,4-galactosyltransferase (GalT) marks the Golgi complex (compare with FAPP1, Fig. 7e). (**b)** Lysosomal associated membrane protein 1 (LAMP1) marks the lysosomal compartment (compare with ATG18, Fig. 7f). (**c)** Early endosome associated 1 (EEA) marks the early endosomal compartment (compare with 2xFYVEhrs, Fig. 7g). Scale bars, 5µm.

Supplementary Figure 8

An over-expression screen of the entire zebrafish Rab family identifies distinct Rab proteins with T-tubule specific localization, and Rab proteins with the ability to perturb T-tubule formation.

(**a**) Rab22a, fourth hit for T-tubule perturbation from Rab screen (continued from Fig. 8). (**b**) Rab8b ectopic tubular "knots". (**c-h**) Validation of top hits for perturbation of the CaaX signal by BODIPY-FLC$_5$ staining. (**c**) Rab6a. (**d**) Rab23. (**e**) Rab11ba. (**f**) Rab4a. (**g**) Rab22a. (**h**)

Rab5c. Note the lack of perturbation by overexpression of rab23 (compare **d** to Fig. 8g). (**i**) Quantitative analysis for perturbation and localization using dominant negative and constitutively active forms of the top hits from the Rab overexpression screen. *p < 0.05, **p < 0.01, ***p < 0.001, ****p < 0.0001. Scale bars, 5µm.

Supplementary Figure 9

An *in vitro* model of T-tubule formation for validation of novel factors in T-tubule development.

(**a**) Rab32b. (**b**) Rab37. (**c**) Rab38a. (**d**) Rab19. (**e**) Caveolin3. (**f**) CaaX. (**g**) Snx8.

Supplementary Video 1

Confocal timelapse series showing initial formation of the skeletal muscle T-tubule system from 18hpf to 31hpf. At 18hpf unstructured tubules can be seen adjacent to the sarcolemma (red arrows). The first tubules adopting regular, reiterated spacing are marked by blue arrows.

Supplementary Video 2

Confocal timelapse series showing initial formation of the skeletal muscle T-tubule system from 30hpf to 39hpf. Transient longitudinal elements can be seen between transverse tubules (blue arrows).

Supplementary Video 3

Serial blockface scanning electron microscope volume in transverse orientation at 48hpf. The sequence pans through serial sections showing heavily stained T-tubules at the Z-lines. It then returns back through the volume displaying a thresholded surface which distinguishes T-tubules, sarcolemma and mitochondria.

Supplementary Video 4

Confocal timelapse series showing a lateral view of a double transgenic zebrafish expressing Lifeact-mKate2 (magenta) and EGFP-CaaX (green). As the actin-rich myofibrils develop, T-tubules form at regular intervals along their length. Structured tubules are invariably associated with myofibrils (blue arrows).

Supplementary Video 5

24hpf EGFP-CaaX zebrafish injected with the low molecular weight tracer Alexa-647-UTP (magenta). At the start of the sequence, tracer is already present on the sarcolemma and in the T-tubules. After several minutes, tracer can be seen in intracellular vesicles (blue arrows).

Methods

Zebrafish husbandry

Fish were maintained according to standard procedures[37] by University of Queensland Biological Resources. All animals were maintained on the Tuebingen/AB (TAB) background.

Stable transgenic fish lines

The new transgenic lines Bact2-Lifeact-mKate2 and Bact2-mKate2-KDEL were made using the Tol2 system according to established methods[38]. However, in order to make our transposase RNA, we generated a new Gateway compatible backbone for in vitro transcription of RNA (pT3TS-Dest_R1-R3) and a new entry clone containing a codon optimized transposase sequence fused to an SV40 nuclear localization sequence on each end (pME-nls-transposase). These were recombined in an LR reaction with p3E-pA[39] to make pT3TS-nls-transposase. This plasmid was linearized with KpnI and XbaI before in vitro transcription with T3 polymerase

as previously described[39, 40]. All transgenics were crossed until Mendelian frequencies were reached, indicative of single genomic integrations. Stable lines were maintained as heterozygotes. Existing lines used in this study were acta1-EGFP-CaaX (Hras)[11], acta1-Lifeact-EGFP[41], acta1-mCherry-CaaX[41] (Table 1).

BODIPY staining

BODIPY-FLC$_5$ and TR vital staining was carried out as previously described[19, 42]. Briefly, embryos were incubated overnight in 5µg/ml BODIPY-FLC$_5$ (Molecular Probes, catalogue number D3521). Embryos were washed for 5min in standard embryo media before being mounted for microscopy.

Intra-cardiac/intra-muscular injection

For fluid phase marker tracing by electron microscopy, approximately 4nl of 10mg/ml unconjugated horse radish peroxidase (Sigma-Aldrich P8375) dissolved in water was injected into the pre-cardiac sinus at 48hpf[43]. After 45 minutes fish were fixed and processed for TEM as described. For fluid phase marker tracing by confocal microscopy, approximately 4nl of 1mM Alexa-647 conjugated UTP (Thermo-Fisher A32763) was injected into the trunk musculature of 16, 24 and 48hpf zebrafish[44] and imaged immediately. For small molecular weight marker tracing by confocal microscopy, approximately 4nl of 1mM Alexa-647 conjugated 10,000MW dextran (Thermo-Fisher D22914) was injected into the trunk muscle of 24hpf zebrafish and imaged immediately.

Confocal Imaging

Confocal imaging of zebrafish was performed on Ziess 710 meta confocal microscopes as previously described[43]. Briefly, zebrafish were mounted in 1% low melting point agarose in

embryo media[37], in either a MatTek dish (for inverted microscopes) or a standard 8cm petri dish for upright microscopes. Objectives used were Zeiss water immersion x40 N/A 1.0 (catalogue number 420762) on upright microscopes or oil immersion x 40 N/A 1.3 (catalogue number 421462) on inverted microscopes. Embryos were anaesthetized in 2.5mM tricaine prior to imaging. Confocal imaging of BHK cells was carried out at 37 °C on a Zeiss Inverted LSM 880 with Airyscan using a x40 Plan Apochromat objective (catalogue number 420762-9800-799). At 18 h post transfection, cell culture medium was replaced with phenol red free DMEM/F12 medium (Invitrogen Australia, 11039-021) containing 10% FBS one hour prior to microscope imaging.

Tissue Culture

BHK cells from a baby hamster kidney fibroblast cell line (ATCC CCL-10), were cultured in DMEM (Life Technologies Australia Pty Ltd Invitrogen, 11995073) supplemented with 10% (vol/vol) FBS (GE Healthcare Australia, SH30084.03) and 1% (vol/vol) L-glutamine (Life Technologies Australia, 25030-081) as previously described[45]. Cells were seeded onto glass bottom dishes and at 70% confluence were transfected with DNA constructs using Lipofectamine 3000 reagents (Life Technologies Australia Pty Ltd Invitrogen, L3000015) according to the manufacturer's instructions. All cells used were between passage 9 and 13 and all cell lines in use in our laboratory are subject to a quarterly mycoplasma testing regime (Sapphire Bioscience, B39032).

Mosaic transgenesis

Plasmids were delivered to recently laid embryos by microinjection of approximately 4nl into the yolk at 15ug/ml without transposase RNA. Embryos were sorted for transgenesis prior to imaging.

Constructs and cloning

New ORFs were generated from cDNA and first cloned into pGemTeasy (Promega). Primers were designed using primer3[46] to the boundary between the ORF and the UTR. Expression plasmids were constructed using the Tol2 kit[39]. New entry clones were made by PCR subcloning from existing plasmids using primers containing gateway compatible sites. The multisite gateway system is designed so as to be able to stitch together three cassettes in the correct order and orientation within a backbone. In order to streamline the production of large numbers of constructs using many of the same cassettes, we used a strategy in which we were able to perform the gateway reaction in reverse. That is, to take one of our final expression clones and replace either the middle cassette, 3' cassette, or both cassettes with the *ccdb* gene. This has the advantage that reactions are able to be performed with a smaller number of component vectors increasing the frequency of correct recombination, and that the largest and most difficult cassettes to recombine (such as promoters) do not need to be recombined in every reaction. In order to do this, we set up gateway reactions with standard volumes and vector concentrations, but only two components; the final expression clone, and the appropriate entry clone containing the *ccdb*/chloramphenicol cassette. In order to perform the LR reaction in reverse, we used BP clonase, transformed into *ccdb* resistant cells, and spread onto plates containing both ampicillin and chloramphicol. In order to substitute both middle and 3' cassettes at the same time, used our new entry vector pDONR_p1-p3 (synthesized by Genscript, U.S.A.). All new constructs have been made available from Addgene and are listed in Supplementary Table 1.

Image processing

In order to avoid bias and ensure reproducibility, we developed a suite of custom macros for ImageJ which we were able to use for the majority of our image processing tasks (Table 2). Full code for all macros is given in Supplementary Macros. For all analysis, a minimum of six cells from a minimum of two fish were imaged per condition. For all data sets, we first used Macro 1 to produce merged .tif files from the native Zeiss .lsm or .czi formats that could be quickly browsed. Where single images are shown, a representative image was selected and then the original confocal file was opened in ImageJ, and the raw 16-bit data from each channel was copied and pasted directly into the RGB channels of Adobe Photoshop. Color-blind compatible images were made by duplicating the red channel into the blue to produce magenta. Brightness and contrast were adjusted as necessary.

Fibre morphometrics from tiled transmission electron microscope images were captured by manual tracing into regions of interest (ROIs) using Macro 2. This macro prevents ROIs from overlapping in the case of fibres by trimming the edges of new ROIs to abut existing ROIs. Myofibrils are trimmed to be within existing fibres, and are automatically named after the parent fibre. Similarly myofibrillar furrow ROIs are trimmed to fall within myofibril ROIs and are named after the parent ROI. Data can then be quickly extracted from the ROI set using the standard measuring tools.

Analysis of perturbation in T-tubule intensity by amplitude was performed in a semi-automated manner. *In vivo* samples and images can be heterogeneous in intensity and quality. However, our mosaic analysis of single over-expressing fibres in an otherwise wildtype provided a robust an internal control, and allowed us to compare domains within individual images, before comparing between images. First, Macro 3 was used to generate .tif images from the original data with enhanced brightness and contrast, and any saturated pixels highlighted. Next, Macro

4 was used to generate sets of "box ROIs" covering arrays of eight T-tubules from adjacent expressing and non-expressing cells. This part of the analysis could not be automated, since the selection of equivalent areas through the midline of each cell was required. Next, Macro 5 was used to extract the amplitude data from the original, raw confocal files using the ROI sets. Similarly, localization of markers to the T-tubule domain was achieved using Macros 6 and 7 to define each localization domain, and Macro 8 to extract the intensity data using the ROI sets. Macros 5 and 8, apply a median filter with a pixel radius of 1 to the raw images before data extraction, to prevent potential noise generated by pixel spikes.

ROI sets were able to be exported to vector based .svg files using the python script "Export ROIs in RoiManager to a SVG file" from the "Python + ImageJ, Fiji Cookbook" at the BioImage Analysis Wiki http://wiki.cmci.info/start

Transmission electron microscopy

Zebrafish were anesthetized with tricaine (Sigma) in E3 and fixed with 2.5% glutaraldehyde in a Pelco BioWave microwave at 80W for 6 min under vacuum in a 2min on, 2min off, 2min on, sequence. The head and tail-tips of the zebrafish embryos were removed and the remaining trunk was re-fixed in 2.5% glutaraldehyde in the microwave using the same sequence. Zebrafish were then processed as described previously[47]. Briefly, samples were washed in PBS and postfixed in 2% OsO4 with 1.5% potassium ferricyanide. Samples were washed in water and incubated in a 1% (w/v) thiocarbohydrazide solution for 20min. Tissue was postfixed again in 2% OsO4, washed in water and stained with 1% uranyl acetate. Tissues was further stained with a lead aspirate solution (20mM lead nitrate, 30mM asparatic acid, pH 5.5), serially dehydrated in acetone, infiltrated with resin and polymerized. Ultrathin sections were cut on a

Leica UC6 ultramicrotome and imaged at 80kV on a JEOL-1011 transmission electron microscope fitted with an Morada 2k x 2k CCD camera under the control of Olympus software.

Large area tiled transmission electron microscopy

Large-area imaging was performed on a Tecnai T12 G2 (FEI) transmission electron microscope at 120kV fitted with a Direct Electron LC-1100 4k x 4k CCD camera using the Navigator program in SerialEM (Mastronade). Images were captured with a pixel size of 8nm and montages were aligned using the blendmont program in IMOD[48]. Images for all time points were captured using the same settings.

3View Serial blockface scanning electron microscopy

Samples for serial blockface sectioning scanning electron microscopy were processed as for transmission electron microscopy. Imaging was performed on a Zeiss Gemini FE-SEM fitted with a Gatan 3view, at 2.25kV, with magnification 7.5k and a pixel size of 5.7nm. Images were captured at a resolution of 5000x5000 (dwell 2), under low vacuum (8Pa) with 50nm sections. Image stacks were aligned using the xfalign program in IMOD and automated segmentation was performed by density-based thresholding in the Isosurface render program in IMOD.

Focussed ion beam electron microscopy

Following glutaraldehyde fixation and washing samples were placed in 2% osmium tetroxide in 0.1M cacodylate buffer and incubated in a Pelco Biowave at 80W for 6 min under vacuum in a 2min on, 2min off, 2min on, sequence. The osmium solution was removed without rinsing and a solution of 2.5% potassium ferricyanide was added and placed into the Pelco BioWave for a further 6 minutes, at 80W, under vacuum on a 2min on, 2min off 2min on, sequence. Samples were then removed and washed in distilled water 6 times for 2mins. Samples were

further incubated in an aqueous filtered solution of 1% thiocarbohydrazide, (6 min under vacuum) in a 2min off 2min on sequence. After rinsing in distilled water in a 6 x 2 min sequence, samples were placed in an aqueous 2% osmium tetroxide for 6 min under vacuum in a 2min on, 2min off, 2min on, sequence. After rinsing in distilled water in a 6 x 2 min sequence, samples were placed in 1% uranyl acetate solution and again irradiated at 80W for 3min. Samples were removed and washed in distilled water in a 6 x 2 min sequence, and dehydrated through an ethanol series (30%, 50%, 70%, 90% and 100% ethanol for 40s at 250W) in the Pelco BioWave, prior to embedding in Durcupan resin. Samples were imaged on an FEI Scios FIB Dual Beam SEM at 1.5kV with a 0.8nA electron beam at a resolution of 3072x2048, with a chamber vacuum of 1 – 2 x 10^{-4} Pa. Slicing was carried out at 30kV with a 1nA Ga^{+} ion beam. Voxel size and slice thickness was 8nm.

Statistical Analyses

Linear, second and third degree polynomial regression equations for mathematical modelling (Fig. 3d-f) were generated using the LINEST function in Excel (Microsoft). A one-tailed T-test was used to compare inter T-tubule distance between fast and slow fibres from *smyhc1*$^{-/-}$ mutants (Fig. 4g; Microsoft Excel, T.TEST function for heteroscedastic data). One tailed T-tests were also used to compare average pixel intensity at the T-tubule domain compared to the inter T-tubule domain (localization data, Fig. 6j, 6m, 7h, 8i and Supplementary Fig. 8i; Microsoft Excel, T.TEST function for heteroscedastic data). Significance was tested on all markers showing >/= 10% increase in intensity at the T-tubule compared to the inter-tubule domain. Two-tailed T-tests were used to compare average pixel intensity in overexpressing cells compared to non-expressing cells (perturbation data, Fig. 8i and Supplementary Fig. 8i) and the extent of perturbation of wildtype vs dominant negative markers (Fig.6m; Microsoft Excel, T.TEST function for heteroscedastic data). One-way ANOVA followed by a Tukey

multiple comparison test was used to compare tubule diameters between *ttn*$^{-/-}$ and wildtype fish in the presence or absence of SR association (Fig, 4k; GraphPad Prism 8).

Mathematical model

The mathematical model was built according to the following assumptions.

i) Each muscle fibre is assumed to be a perfect cylinder, where fibre cross-sectional area is given by the equation for the area of a circle πr^2, where r = radius. Note that fibre diameter and cross-sectional area are both used in the existing literature as valid measurements of fibre dimensions in muscle cellularity studies. Our rationale in choosing fibre diameter as an input parameter rather than cross-sectional area was to provide the simplest and most applicable model. In our model, fibre cross sectional area is calculated from fibre diameter (D) where:

$$\pi \left(\frac{D}{2}\right)^2$$

ii) Myofibril cross-sectional area is a function of fibre cross sectional area and can be calculated from the linear regression equation shown in Fig 3d ($y = 0.95x - 13.55$), where x is muscle fibre cross sectional area. Combining equations for fibre cross sectional area and myofibril cross sectional area allows calculation of myofibril cross sectional area from fibre diameter (D).

$$0.95\pi \left(\frac{D}{2}\right)^2 - 13.55$$

iii) The T-tubules track through the splits or “furrows” in the myofibrils, such that at the level of each and every Z-line within a fibre, the total combined length of the myofibrillar furrows in transverse section (illustrated by the red lines in Fig.2k) will be equal to the total combined length of the associated T-tubules. Moreover, total linear furrow distance can be predicted from the cross sectional area of the myofibrils within a fibre by the equation $y = 1.26x + 6.06$ (Fig.

3e). Combining equations for myofibril cross sectional area and total linear furrow distance allows calculation of the length of T-tubule associated with each single Z-line within a muscle fibre, using the diameter area of the fibre (*D*):

$$1.26\left[0.95\pi\left(\frac{D}{2}\right)^2-13.55\right]+6.06$$

iv) The number of "units" given by this equation is equal to the number of Z-lines within a muscle fibre. This value can be calculated from fibre length (*L*) and sarcomere length (*s*) using *L*/*s*. Therefore the total length of Z-line associated T-tubules within a single muscle fibre of length (L) and diameter (D) is given by:

$$\frac{L}{s}\times 1.26\left[0.95\pi\left(\frac{D}{2}\right)^2-13.55\right]+6.06$$

v) T-tubules are an elliptical tube with a circumference given by Ramanujan's approximation for the perimeter of an ellipse (*p*) where *a* and *b* define the major and minor axes, measured from the centre to the perimeter (e.g. in the case of a circle, both *a* and *b* would be equal to the radius):

$$p\approx\pi[3(a+b)-\sqrt{(3a+b)(a+3b)}]$$

In our model Ramanujan's approximation becomes the following, where *d*1 and *d*2 are the major and minor axes of T- diameters:

$$\pi\left(3\left[\frac{d1}{2}+\frac{d2}{2}\right]-\sqrt{\left[3\cdot\frac{d1}{2}+\frac{d2}{2}\right]\left[\frac{d1}{2}+3\cdot\frac{d2}{2}\right]}\right)$$

Dividing by 1000, to convert the output units from nm to µm gives:

$$\frac{1}{1000}\times\pi\left(3\left[\frac{d1}{2}+\frac{d2}{2}\right]-\sqrt{\left[3\cdot\frac{d1}{2}+\frac{d2}{2}\right]\left[\frac{d1}{2}+3\cdot\frac{d2}{2}\right]}\right)$$

vi) The total surface area of the T-tubules within a single muscle fibre of length (*L*) and diameter (*D*) is given by combining the equations in (iv) and (v), using the major and minor axes of the cross section of an elliptical T-tubule (*d*1 and *d*2) and sarcomere length (*s*):

$$\frac{1}{1000}\times\pi\left(3\left[\frac{d1}{2}+\frac{d2}{2}\right]-\sqrt{\left[3\cdot\frac{d1}{2}+\frac{d2}{2}\right]\left[\frac{d1}{2}+3\cdot\frac{d2}{2}\right]}\right)\times\frac{L}{s}\times\ 1.26\left[0.95\pi\left(\frac{D}{2}\right)^2-13.55\right]+6.06$$

Which simplifies to:

$$\frac{3L\pi(3d1+3d2-\sqrt{(3d1+d2)(d1+3d2)})(399\pi D^2-14684)}{8000000s}$$

Using the values calculated from our experimental data of d1= 59.24nm, d2 = 96.47nm, s = 1.9µm, this simplifies to:

$$\frac{157.939995L\pi(1.197\pi D^2-44.052)}{15200}$$

And still further, if cross sectional area (*C*) is preferred as an input parameter, which may be of use to some investigators:

$$\frac{157.939995L\pi(1.197C)-11.013}{3800}$$

vi) The surface area of plasma membrane (sarcolemma) is calculated using equations for the area of a circle πr^2, where *D* is the fibre diameter (and *D*/2 is the radius, *r*):

$$\pi\left(\frac{D}{2}\right)^2$$

and has a circumference given by $2\pi r$:

$$2\pi\frac{D}{2}$$

Multiplying the cross sectional area by 2 gives the surface area of each of the fibre ends, and multiplying the circumference by the fibre length (L), gives the remainder of the surface area. The total surface area, excluding the T-tubules, is therefore given by:

$$2\pi\left(\frac{D}{2}\right)^2 + 2\pi L\left(\frac{D}{2}\right)$$

Application of the mathematical model to 48hpf, 5dpf 10dpf and adult zebrafish.

In order to calculate the surface areas of the T-tubule and sarcolemma at 48hpf, 5dpf and 10dpf, values for fibre length (L) were 90.23µm, 107.77µm and 158.83µm respectively, and were calculated using the regression equation for somite width ($y = 0.2x^3 - 2.6x^2 + 17x + 65$; Fig 3f) for values of $x = 2$, $x = 5$ and $x = 10$. Values for maximum fibre diameter (D) were 15.64µm, 19.23µm and 26.72µm respectively (directly measured cross-sectional areas of 192.04µm^2, 290.42µm^2 and 560.86µm^2) taken from the empirically derived data shown in Fig 3a-c. Note that these calculations were based on maximum fibre size (rather than the mean size or animal age) since new fibres are continuously added to the myotome and existing fibres grow at different rates (see cellularity profile histograms in Supplementary Fig. 3a-c). To apply this model to the largest fibres found in adult zebrafish we took approximate measurements from the zebrafish atlas images at (http://bio-atlas.psu.edu/zf/view.php?s=220&atlas=18; http://bio-atlas.psu.edu/zf/view.php?s=275&atlas=17). The largest fibres we found in this data set were approximately 580µm in length and 40µm in diameter. Applying values of L = 580µm and D = 40µm, gave values of 113083 : 75398µm^2; (T-system : sarcolemma) which corresponds to approximately 1.5x. The graphs in Fig. 3h & i show the consequences of scaling fibre length and diameter up to the maximal values measured from 1 year old fish of L = 580µm and D = 40µm (cross sectional area = 1256.64µm^2).

In order to find the point at which the surface area of the sarcolemma and the surface area of the T-tubules are equal (the intercept, shown as a dotted line in Fig. 3h and i), we equated the formulas as follows:

$$2\pi\left(\frac{D}{2}\right)^2 + 2\pi L\left(\frac{D}{2}\right) = \frac{157.939995L\pi(1.197\pi D^2 - 44.052)}{15200}$$

Solving for L gives:

$$L = -\frac{7600D^2}{15200D - 189.05417\pi D^2 + 6957.57265}$$

Solving for D gives:

$$D = \frac{-47752.20833L \pm \sqrt{47752.20833^2L^2 - 87431.43661L(23876.10416 - 1865.88990L)}}{2(23876.10416 - 1865.88990L)}$$

CRISPR/Cas9

Guide RNAs were designed using CRISPRscan software[49]. To generate vectors for sgRNA production we modified the pT7-gRNA vector[50] to include a *ccdb* cassette vector (pT7-gRNA-*ccdb*) for negative selection to improve cloning efficiency, which in hands, was low with the original. sgRNA sequences were incorporated by one-step oligo annealing and ligation using BsmBI as described[50]. DNA templates were generated from these plasmids using a 100µl PCR (98° for 5s followed by 35 cycles of 98° for 5s, 55° for 5s, 72° for 20s) and the generic primers sgRNA_F1 (5'-GCAGCTGGCACGACAGGTTTCC-3') sgRNA_R1 (5'-AAAAAAAAAGCACCGACTCGGTGCCACTTTTTCAAGTT-3'). sgRNAs were generated from the purified amplicons using the Ambion MegaShortScript kit (quarter size reactions). sgRNAs were complexed with EnGen Spy Cas9 NLS protein (New England Biolabs M0646T)

for 5 minutes at 37°C before injection of approximately 4nl into the yolk at the one cell stage. Gene-specific sgRNAs were co-injected with an sgRNA targeting tyrosinase[50], to allow selection of founders possessing the highest cutting frequencies. The molar ratio of Cas9 to total sgRNA was 1:1.5. Founders were outcrossed and F1 animals were genotyped by sequencing to identify null mutations and mutant lines were maintained as heterozygotes. sgRNA sequences used were tyr_80[50] (5'-GGACTGGAGGACTTCTGGGG-3'), smyhc1_977 (5'-CAGTGGCAATCAACTCTTCGG-3') and ttn.1_C3[51] (5'-TACTGGGGAATTCAGTGAAGG-3').

Knockout fish lines

The slow myosin heavy chain mutant generated in this study contains a 2bp deletion in the slow myosin heavy chain open reading frame (AACGTCAGTGGCAATCAACT[CTdel]TCGGCATCATCAATCGATGC). The titin mutant *ttn.1* generated in this study contains a 2bp deletion/7bp insertion in the titin open reading frame (TGGGTACTGGGGAATTCAGT[GAdel]/[AGTATGGin] AGGCAGTATGGAAACTGCAC)

References

1. Betz, R.C. *et al.* Mutations in CAV3 cause mechanical hyperirritability of skeletal muscle in rippling muscle disease. *Nat Genet* **28**, 218-219 (2001).
2. Bitoun, M. *et al.* Mutations in dynamin 2 cause dominant centronuclear myopathy. *Nat Genet* **37**, 1207-1209 (2005).
3. Laporte, J. *et al.* A gene mutated in X-linked myotubular myopathy defines a new putative tyrosine phosphatase family conserved in yeast. *Nat Genet* **13**, 175-182 (1996).
4. Liu, J. *et al.* Dysferlin, a novel skeletal muscle gene, is mutated in Miyoshi myopathy and limb girdle muscular dystrophy. *Nat Genet* **20**, 31-36 (1998).
5. Minetti, C. *et al.* Impairment of caveolae formation and T-system disorganization in human muscular dystrophy with caveolin-3 deficiency. *Am J Pathol* **160**, 265-270 (2002).
6. Nicot, A.-S. *et al.* Mutations in amphiphysin 2 (BIN1) disrupt interaction with dynamin 2 and cause autosomal recessive centronuclear myopathy. *Nat Genet* **39**, 1134-1139 (2007).

7. Flucher, B.E., Phillips, J.L., Powell, J.A., Andrews, S.B. & Daniels, M.P. Coordinated development of myofibrils, sarcoplasmic reticulum and transverse tubules in normal and dysgenic mouse skeletal muscle, in vivo and in vitro. *Dev Biol* **150**, 266-280 (1992).
8. Franzini Armstrong, C. Simultaneous maturation of transverse tubules and sarcoplasmic reticulum during muscle differentiation in the mouse. *Dev Biol* **146**, 353-363 (1991).
9. Jayasinghe, I.D. & Launikonis, B.S. Three-dimensional reconstruction and analysis of the tubular system of vertebrate skeletal muscle. *J Cell Sci* **126**, 4048-4058 (2013).
10. Lee, E. *et al.* Amphiphysin 2 (Bin1) and T-Tubule Biogenesis in Muscle. *Science* **297**, 1193-1196 (2002).
11. Williams, R.J. *et al.* The in vivo performance of an enzyme-assisted self-assembled peptide/protein hydrogel. *Biomaterials* (2011).
12. Sanger, J.W., Wang, J., Fan, Y., White, J. & Sanger, J.M. Assembly and Dynamics of Myofibrils. *J Biomed Biotechnol* **2010**, 1-9 (2010).
13. Patterson, S. & Goldspink, G. Mechanism of myofibril growth and proliferation in fish muscle. *J Cell Sci* **22**, 607-616 (1976).
14. Griffiths, G., Back, R. & Marsh, M. A quantitative analysis of the endocytic pathway in baby hamster kidney cells. *J Cell Biol* **109**, 2703-2720 (1989).
15. Riedl, J. *et al.* Lifeact: a versatile marker to visualize F-actin. *Nature Methods* **5**, 605-607 (2008).
16. Jinek, M. *et al.* A programmable dual-RNA-guided DNA endonuclease in adaptive bacterial immunity. *Science* **337**, 816-821 (2012).
17. Elworthy, S., Hargrave, M., Knight, R., Mebus, K. & Ingham, P.W. Expression of multiple slow myosin heavy chain genes reveals a diversity of zebrafish slow twitch muscle fibres with differing requirements for Hedgehog and Prdm1 activity. *Development (Cambridge, England)* **135**, 2115-2126 (2008).
18. Horowits, R. & Podolsky, R.J. The positional stability of thick filaments in activated skeletal muscle depends on sarcomere length: evidence for the role of titin filaments. *J Cell Biol* **105**, 2217-2223 (1987).
19. Lim, Y.-W. *et al.* Caveolae Protect Notochord Cells against Catastrophic Mechanical Failure during Development. *Curr Biol* **27**, 1968-1981.e1967 (2017).
20. Caplan, S. A tubular EHD1-containing compartment involved in the recycling of major histocompatibility complex class I molecules to the plasma membrane. *EMBO J* **21**, 2557-2567 (2002).
21. Pant, S. *et al.* AMPH-1/Amphiphysin/Bin1 functions with RME-1/Ehd1 in endocytic recycling. *Nat Cell Biol* **11**, 1399-1410 (2009).
22. Rosemblatt, M., Hidalgo, C., Vergara, C. & Ikemoto, N. Immunological and biochemical properties of transverse tubule membranes isolated from rabbit skeletal muscle. *J Biochem* **256**, 8140-8148 (1981).
23. Kremer, K. *et al.* An Overexpression Screen of Toxoplasma gondii Rab-GTPases Reveals Distinct Transport Routes to the Micronemes. *PLOS Pathogens* **9**, e1003213 (2013).
24. Chan, C.-C. *et al.* Systematic Discovery of Rab GTPases with Synaptic Functions in Drosophila. *Curr Biol* **21**, 1704-1715 (2011).
25. Young, J. *et al.* Regulation of microtubule-dependent recycling at the trans-Golgi network by Rab6A and Rab6A'. *Mol Biol Cell* **16**, 162-177 (2005).
26. Chavrier, P., Parton, R.G., Hauri, H.P., Simons, K. & Zerial, M. Localization of low molecular weight GTP binding proteins to exocytic and endocytic compartments. *Cell* **62**, 317-329 (1990).

27. Kauppi, M. *et al.* The small GTPase Rab22 interacts with EEA1 and controls endosomal membrane trafficking. *J Cell Sci* **115**, 899-911 (2002).
28. Ullrich, O., Reinsch, S., Urbé, S., Zerial, M. & Parton, R.G. Rab11 regulates recycling through the pericentriolar recycling endosome. *J Cell Biol* **135**, 913-924 (1996).
29. Van Der Sluijs, P. *et al.* The small GTP-binding protein rab4 is associated with early endosomes. *Proc Natl Acad Sci USA* **88**, 6313-6317 (1991).
30. Wang, J.T.H. *et al.* The SNX-PX-BAR family in macropinocytosis: the regulation of macropinosome formation by SNX-PX-BAR proteins. *PloS one* **5**, e13763 (2010).
31. Posey, A.D. *et al.* EHD1 mediates vesicle trafficking required for normal muscle growth and transverse tubule development. *Developmental Biology* **387**, 179-190 (2014).
32. Johannes, L., Parton, R.G., Bassereau, P. & Mayor, S. Building endocytic pits without clathrin. *Nat Rev Mol Cell Biol* **16**, 311-321 (2015).
33. Lakshminarayan, R. *et al.* Galectin-3 drives glycosphingolipid-dependent biogenesis of clathrin-independent carriers. *Nat Cell Biol* **16**, 595-606 (2014).
34. Ketel, K. *et al.* A phosphoinositide conversion mechanism for exit from endosomes. *Nature* (2016).
35. Millar, C.A., Powell, K.A., Hickson, G.R., Bader, M.F. & Gould, G.W. Evidence for a role for ADP-ribosylation factor 6 in insulin-stimulated glucose transporter-4 (GLUT4) trafficking in 3T3-L1 adipocytes. *Journal of biochemistry* **274**, 17619-17625 (1999).
36. Cooper, M.S. *et al.* Visualizing morphogenesis in transgenic zebrafish embryos using BODIPY TR methyl ester dye as a vital counterstain for GFP. *Developmental dynamics : an official publication of the American Association of Anatomists* **232**, 359-368 (2005).
37. Westerfield, M. *The zebrafish book: a guide for the laboratory use of zebrafish (Danio rerio)*. (2007).
38. Kawakami, K. *et al.* A Transposon-Mediated Gene Trap Approach Identifies Developmentally Regulated Genes in Zebrafish. *Dev Cell* **7**, 133-144 (2004).
39. Kwan, K.M. *et al.* The Tol2kit: a multisite gateway-based construction kit for Tol2 transposon transgenesis constructs. *Dev Dyn* **236**, 3088-3099 (2007).
40. Don, E.K. *et al.* A Tol2 Gateway-Compatible Toolbox for the Study of the Nervous System and Neurodegenerative Disease. *Zebrafish* **14**, 69-72 (2017).
41. Berger, J. *et al.* Loss of Tropomodulin4 in the zebrafish mutant trage causes cytoplasmic rod formation and muscle weakness reminiscent of nemaline myopathy. *Dis Model Mech* **7**, 1407-1415 (2014).
42. Lim, Y.-W. *et al.* Caveolae Protect Notochord Cells against Catastrophic Mechanical Failure during Development. *Current biology : CB* **27**, 1968-1981.e1967 (2017).
43. Hall, T.E. *et al.* The zebrafish candyfloss mutant implicates extracellular matrix adhesion failure in laminin 2-deficient congenital muscular dystrophy. *Proc Natl Acad Sci USA* **104**, 7092-7097 (2007).
44. Hall, T.E. *et al.* Cellular rescue in a zebrafish model of congenital muscular dystrophy type 1A. *npj Regenerative Medicine* **4**, 1-13 (2019).
45. Ariotti, N. *et al.* Modular Detection of GFP-Labeled Proteins for Rapid Screening by Electron Microscopy in Cells and Organisms. *Developmental cell* **35**, 513-525 (2015).
46. Untergasser, A. *et al.* Primer3—new capabilities and interfaces. *Nucleic Acids Res* **40**, e115-e115 (2012).
47. Herms, A. *et al.* Cell-to-cell heterogeneity in lipid droplets suggests a mechanism to reduce lipotoxicity. *Curr Biol* **23**, 1489-1496 (2013).
48. Kremer, J.R., Mastronarde, D.N. & McIntosh, J.R. Computer visualization of three-dimensional image data using IMOD. *J Struct Biol* **116**, 71-76 (1996).

49. Moreno-Mateos, M.A. *et al.* CRISPRscan: designing highly efficient sgRNAs for CRISPR-Cas9 targeting in vivo. *Nature Methods* **12**, 982-988 (2015).
50. Jao, L.-E., Wente, S.R. & Chen, W. Efficient multiplex biallelic zebrafish genome editing using a CRISPR nuclease system. *Proc Natl Acad Sci USA* **110**, 13904-13909 (2013).
51. Zou, J. *et al.* An internal promoter underlies the difference in disease severity between N- and C-terminal truncation mutations of Titin in zebrafish. *eLife* **4**, e09406 (2015).

Table 1. Transgenic and mutant zebrafish lines used in this study

	Reference	**Allele number**
bact2-Lifeact-mKate2	This study	uq3rp
bact2-mKate2-KDEL	This study	uq4rp
Slow myosin heavy chain 1 knockout	This study	uq20rp
Titin.1 knockout	This study	uq21rp
acta1-EGFP-CaaX (Hras)	11	pc10

Table 2. Software and algorithms used in this study

Macro or Algorithm	**Reference**
GEN_Split_to_tif_CZI_AND_LSM.ijm	This study
GEN_Morphometrics.ijm	This study
GEN_Split_to_green_and_blue_highlight_saturated.ijm	This study
TT_GET_box_ROIs_for_amplitude_comparison.ijm	This study
TT_perturbation_process.ijm	This study
TT_GET_circle_ROIs_for_localisation_comparison.ijm	This study
GEN_Put_circle.ijm	This study
TT_localisation_comparison_process.ijm	This study
ROI to .svg (Python script)	BioImage Analysis Wiki

Figure 1

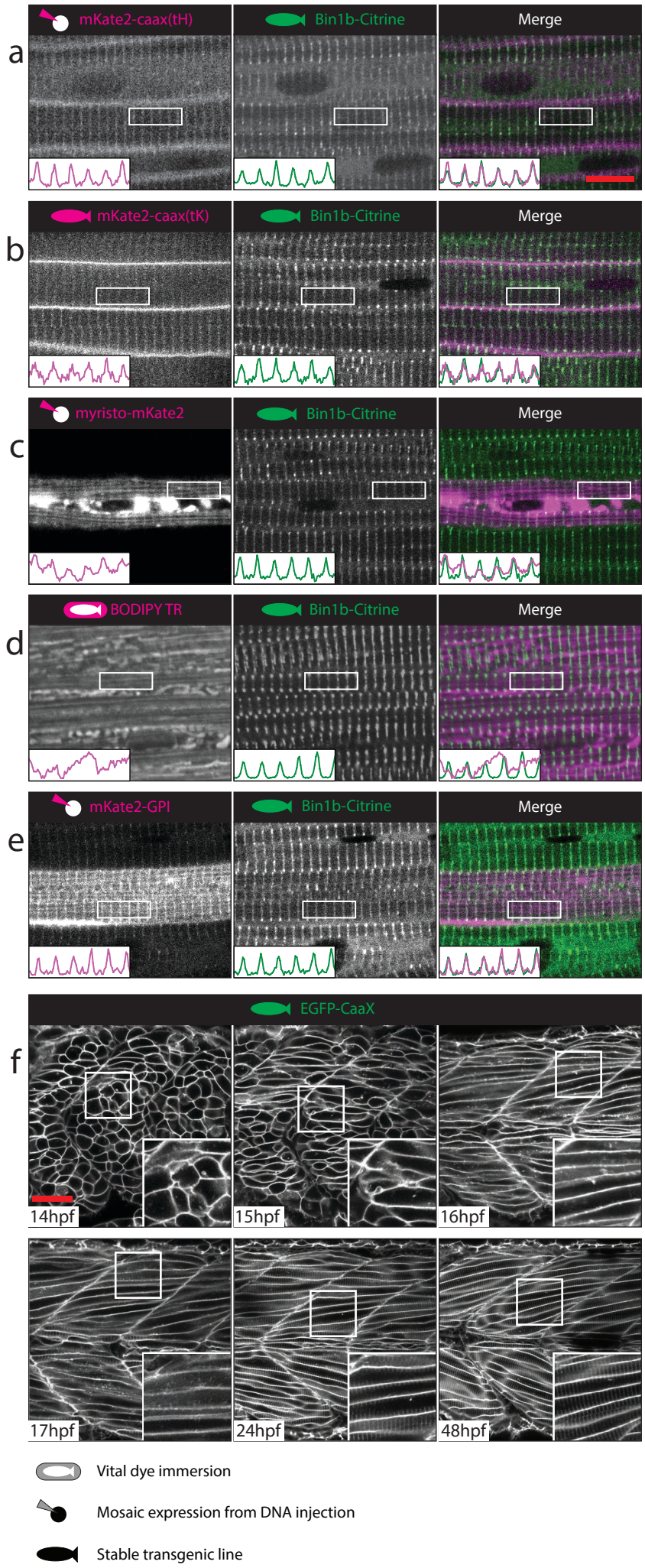
a
mKate2-caax(tH)
Bin1b-Citrine
Merge
b
mKate2-caax(tK)
Bin1b-Citrine
Merge
c
myristo-mKate2
Bin1b-Citrine
Merge
d
BODIPY TR
Bin1b-Citrine
Merge
e
mKate2-GPI
Bin1b-Citrine
Merge
f
EGFP-CaaX
14hpf
15hpf
16hpf
17hpf
24hpf
48hpf
Vital dye immersion
Mosaic expression from DNA injection
Stable transgenic line

Supplementary Figure 1, related to Figure 1

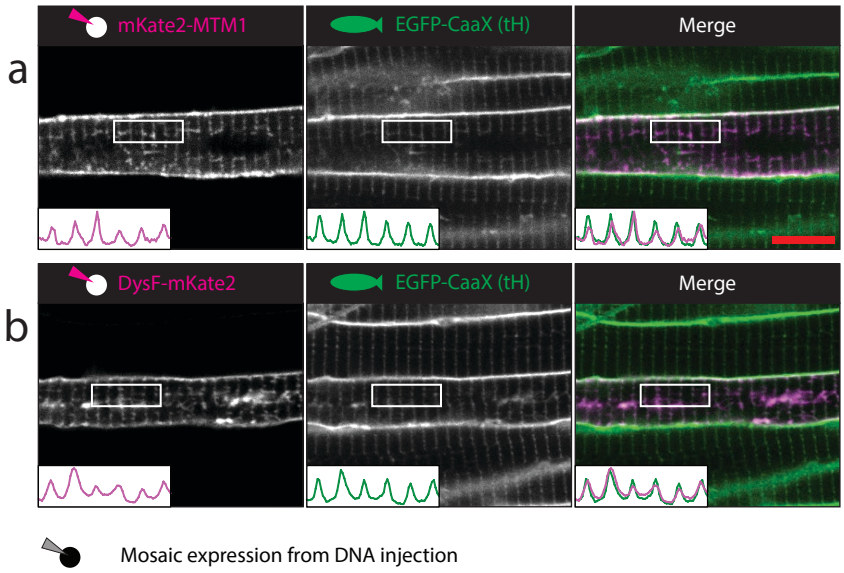

Figure 2

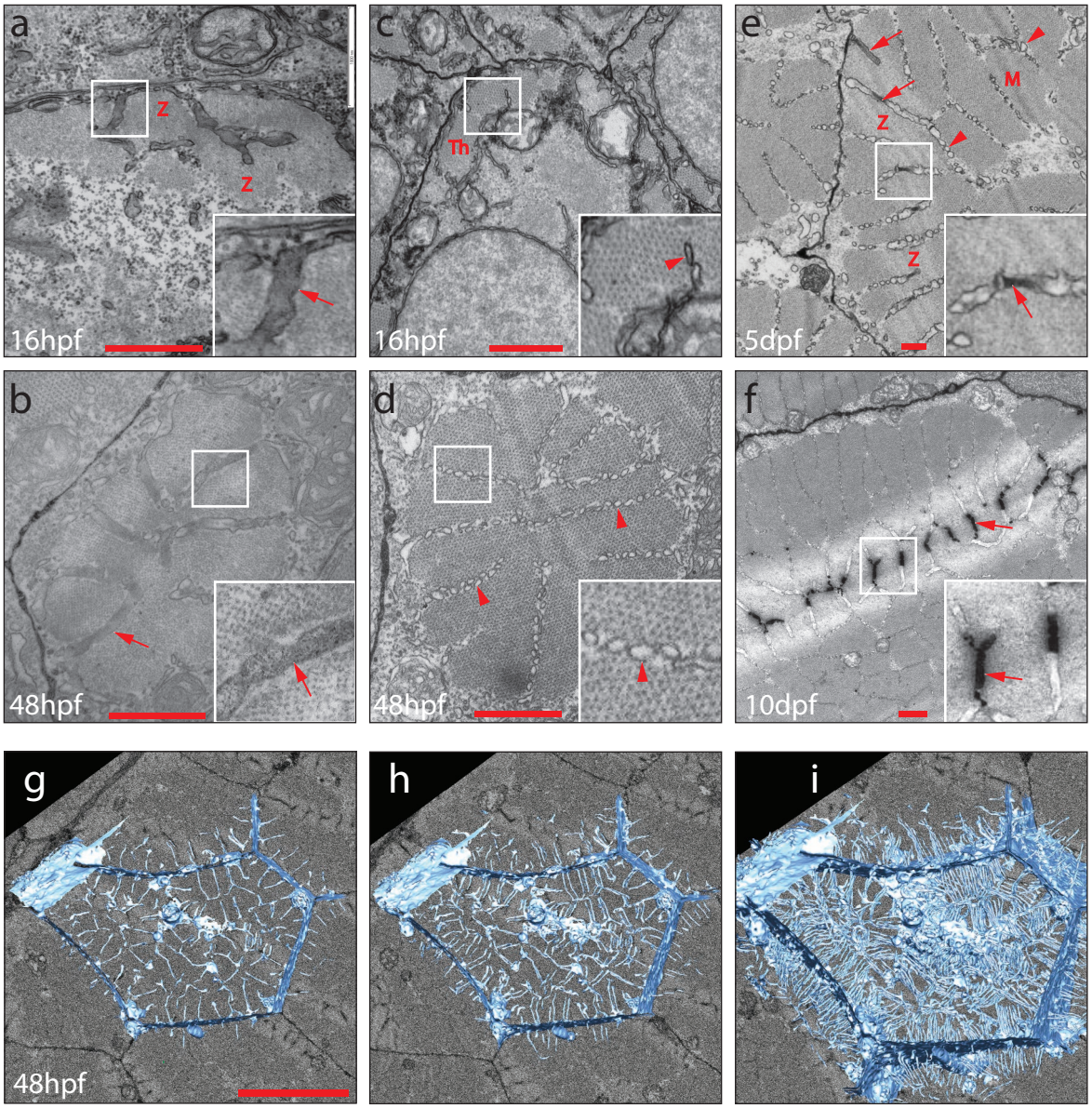
a
Z
Z
16hpf
c
Th
16hpf
e
M
Z
Z
5dpf
b
48hpf
d
48hpf
f
10dpf
g
48hpf
h
i

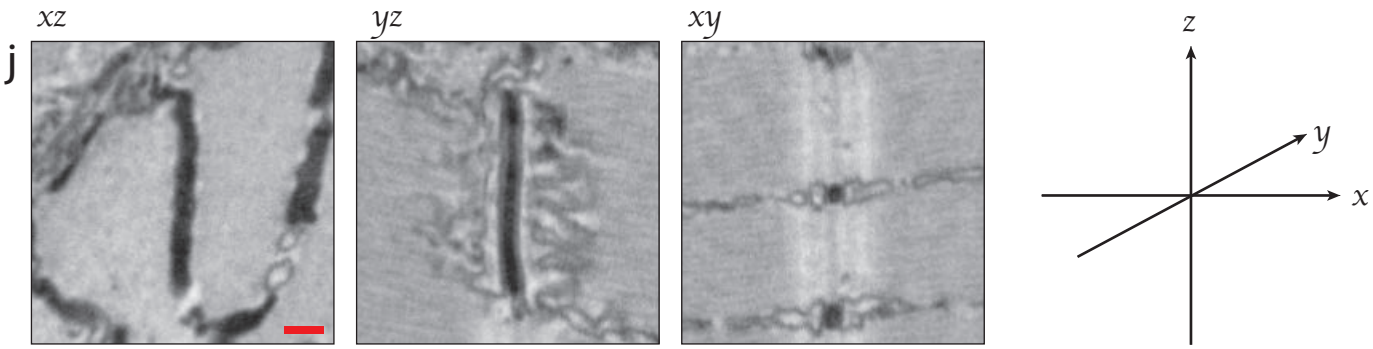
j
xz
yz
xy
z
y
x

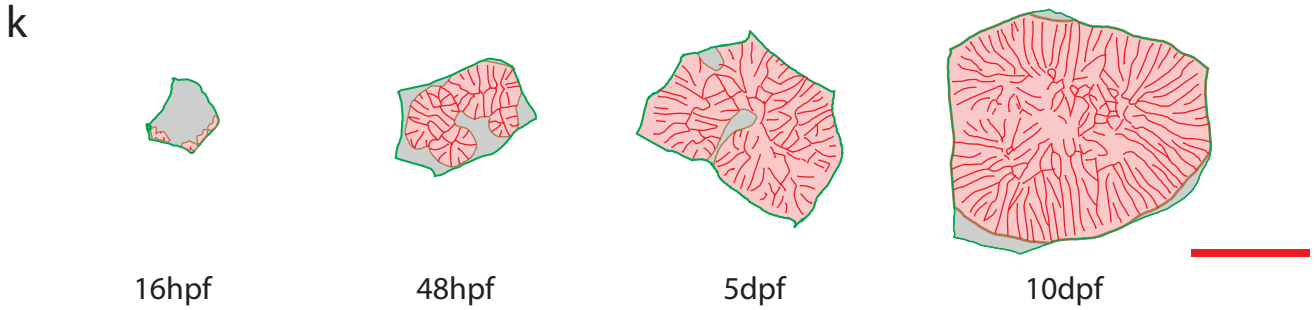
k
16hpf
48hpf
5dpf
10dpf

Figure 3

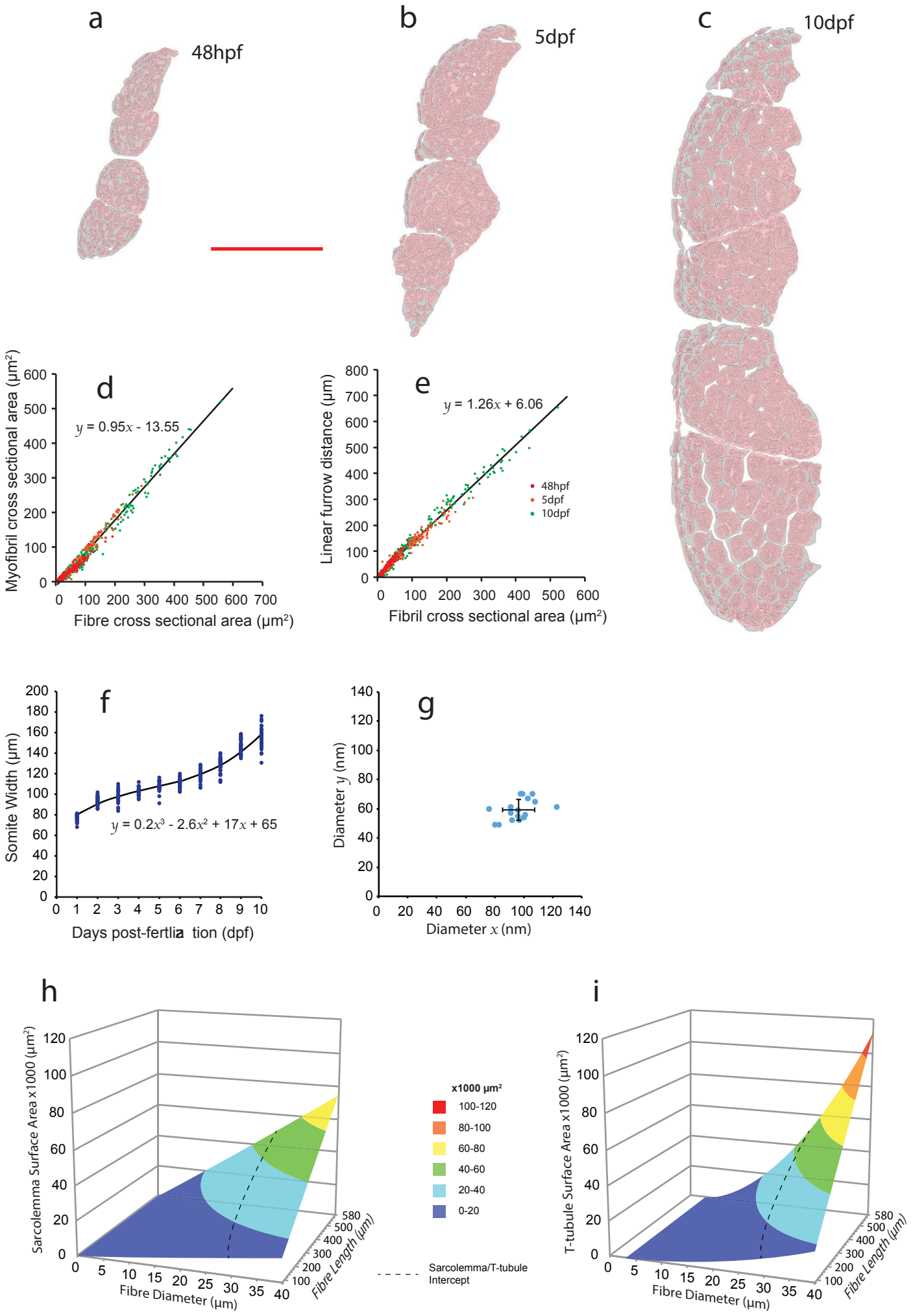
a
48hpf
b
5dpf
c
10dpf
d
y = 0.95x - 13.55
Myofibril cross sectional area (µm²)
Fibre cross sectional area (µm²)
e
y = 1.26x + 6.06
Linear furrow distance (µm)
Fibril cross sectional area (µm²)
48hpf
5dpf
10dpf
f
y = 0.2x³ - 2.6x² + 17x + 65
Somite Width (µm)
Days post-fertlia tion (dpf)
g
Diameter y (nm)
Diameter x (nm)
h
Sarcolemma Surface Area x1000 (µm²)
Fibre Diameter (µm)
Fibre Length (µm)
x1000 µm²
100-120
80-100
60-80
40-60
20-40
0-20
Sarcolemma/T-tubule Intercept
i
T-tubule Surface Area x1000 (µm²)
Fibre Diameter (µm)
Fibre Length (µm)

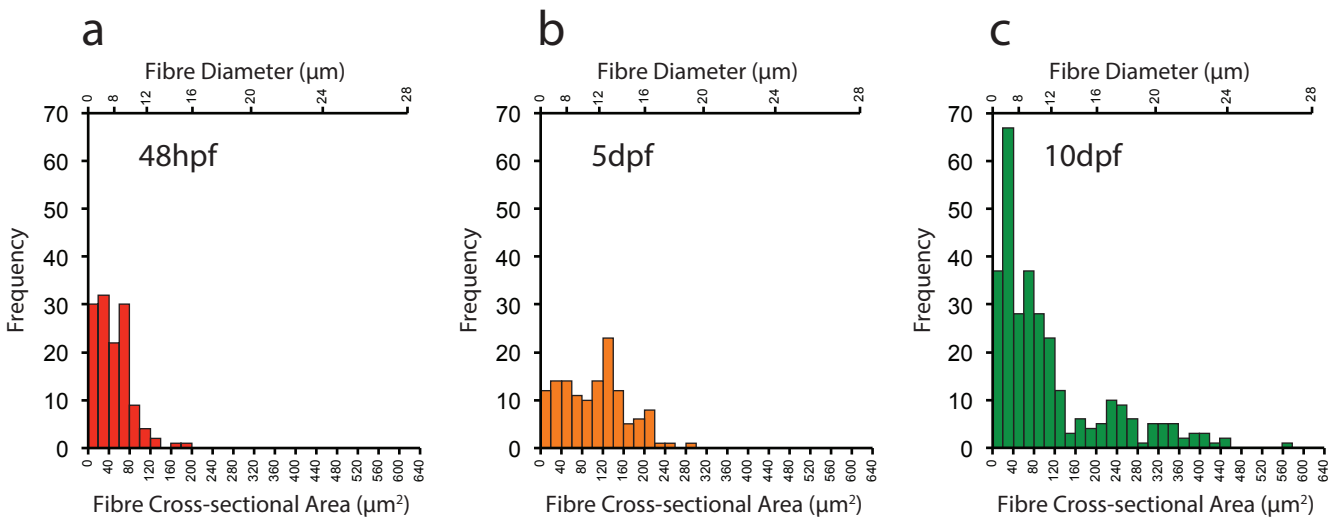

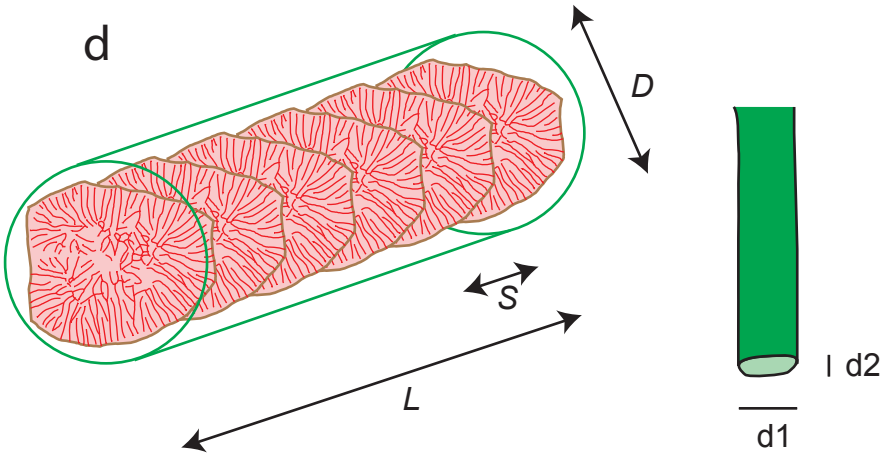

L = Fibre length (µm)
D = Fibre diameter (µm)
s = Sarcomere length (µm)
d1 = T-tubule diameter 1 (nm)
d2 = T-tubule diameter 2 (nm)

e

$$\frac{1}{1000} \times \pi \left(3\left[\frac{d1}{2}+\frac{d2}{2}\right] - \sqrt{\left[3\cdot\frac{d1}{2}+\frac{d2}{2}\right]\left[\frac{d1}{2}+3\cdot\frac{d2}{2}\right]} \right) \times \frac{L}{s} \times 1.26\left[0.95\left(\pi\left(\frac{D}{2}\right)^2\right)-13.55\right]+6.06$$

Conversion from nm to µm for tubule perimeter

Perimeter of T-tubule cross-sectional ellipse (Ramanujan's approximation)

Number of sarcomeric units (fibre length/sarcomere length)

Total linear furrow distance per sarcomere (TT length; see alse Fig. 3e)

Myofibril cross sectional area (see also Fig. 3d)

Fibre cross sectional area

f

$$\frac{3L\pi(3d1+3d2-\sqrt{(3d1+d2)(d1+3d2)})(399\pi D^2-14684)}{8000000s}$$

g

$$\frac{157.939995L\pi(1.197\pi D^2)-44.052}{15200}$$

Figure 4

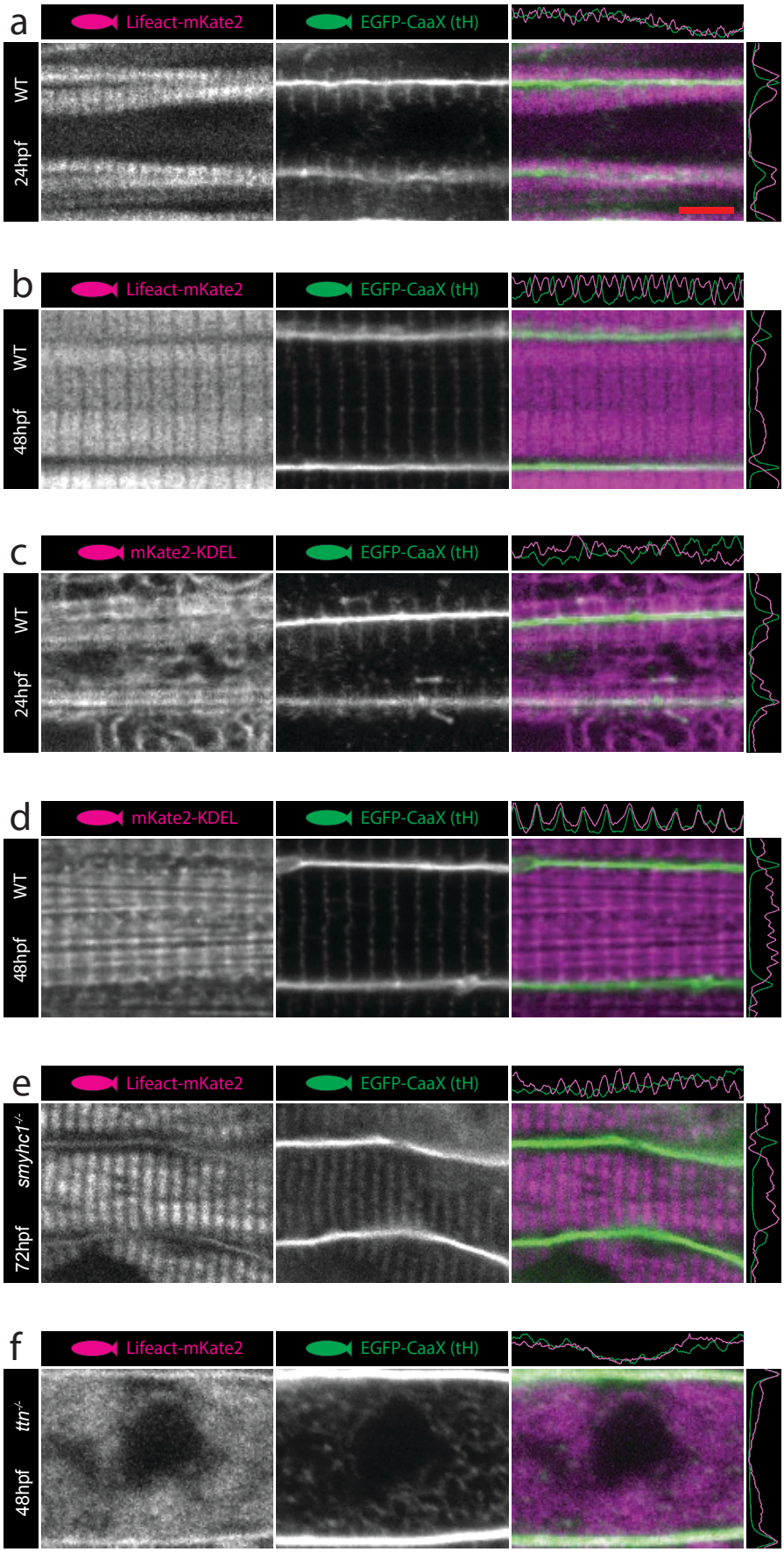
a
Lifeact-mKate2
EGFP-CaaX (tH)
WT
24hpf
b
Lifeact-mKate2
EGFP-CaaX (tH)
WT
48hpf
c
mKate2-KDEL
EGFP-CaaX (tH)
WT
24hpf
d
mKate2-KDEL
EGFP-CaaX (tH)
WT
48hpf
e
Lifeact-mKate2
EGFP-CaaX (tH)
smyhc1-/-
72hpf
f
Lifeact-mKate2
EGFP-CaaX (tH)
ttn-/-
48hpf
Mosaic expression from DNA injection
Stable transgenic line

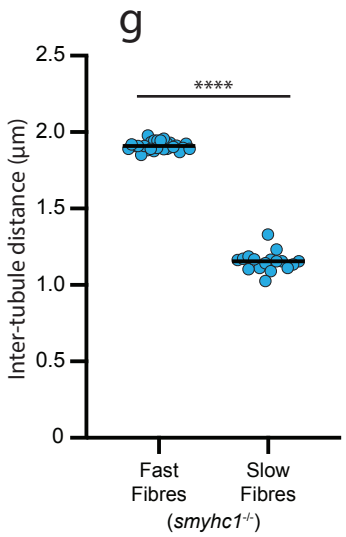
g
Inter-tubule distance (µm)
2.5
2.0
1.5
1.0
0.5
0
****
Fast Fibres
Slow Fibres
(smyhc1-/-)

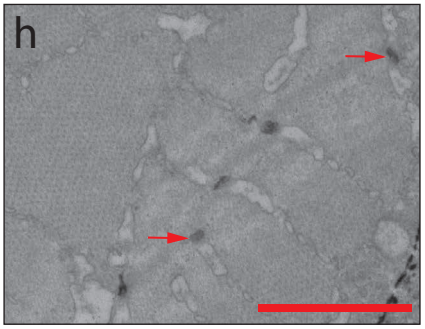
h

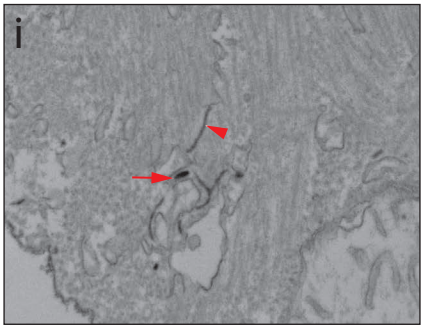
i

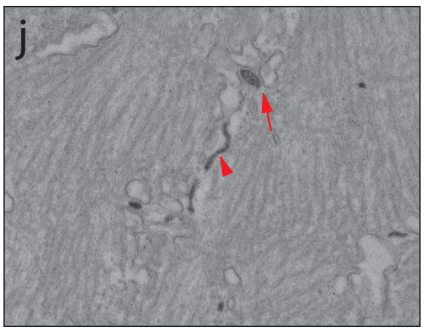
j

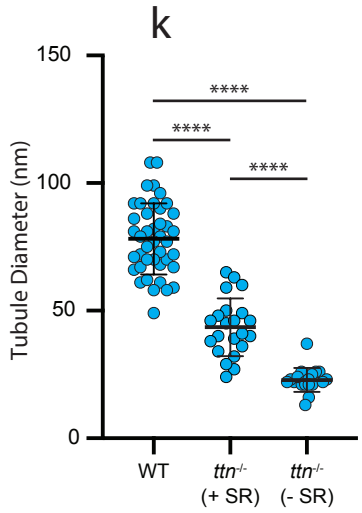
k
Tubule Diameter (nm)
150
100
50
0
****
****
****
WT
ttn-/- (+ SR)
ttn-/- (- SR)

Supplementary Figure 4
related to Figure 4

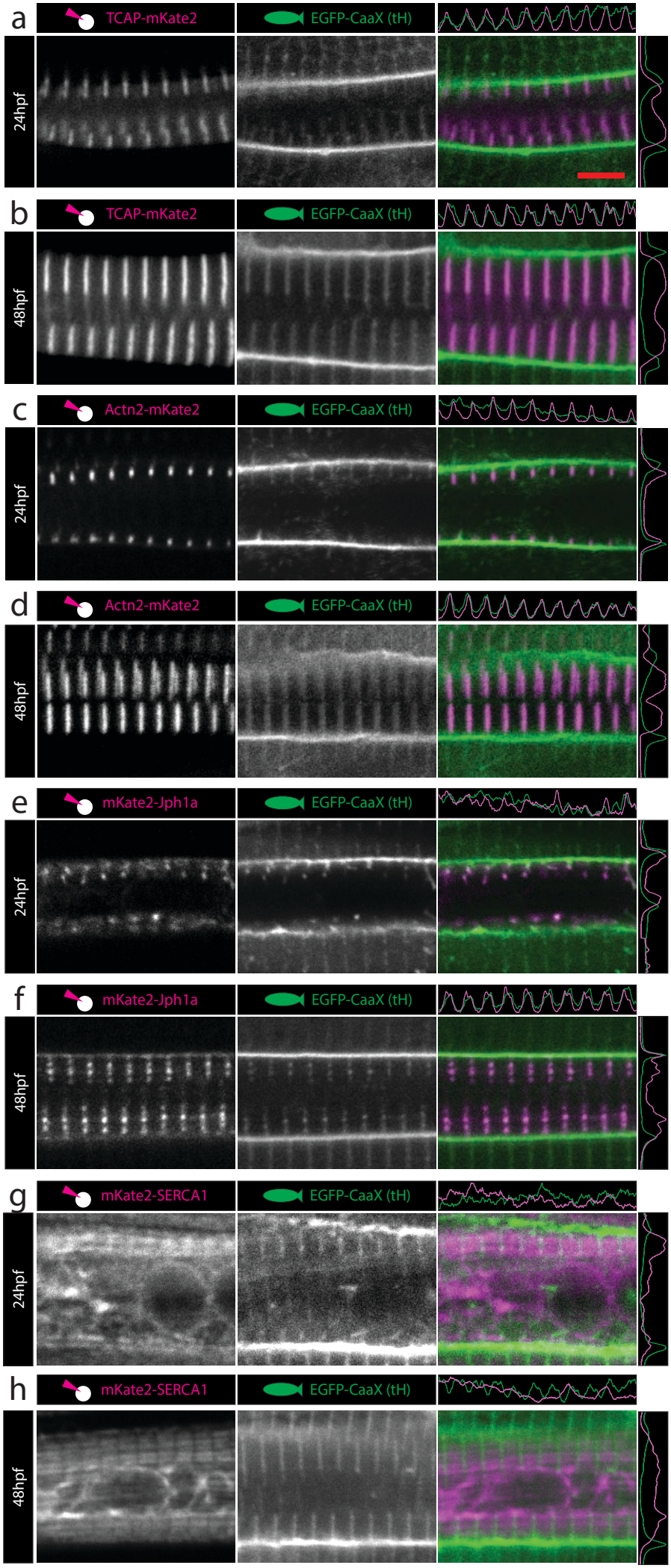

Mosaic expression from DNA injection

Stable transgenic line

Figure 5

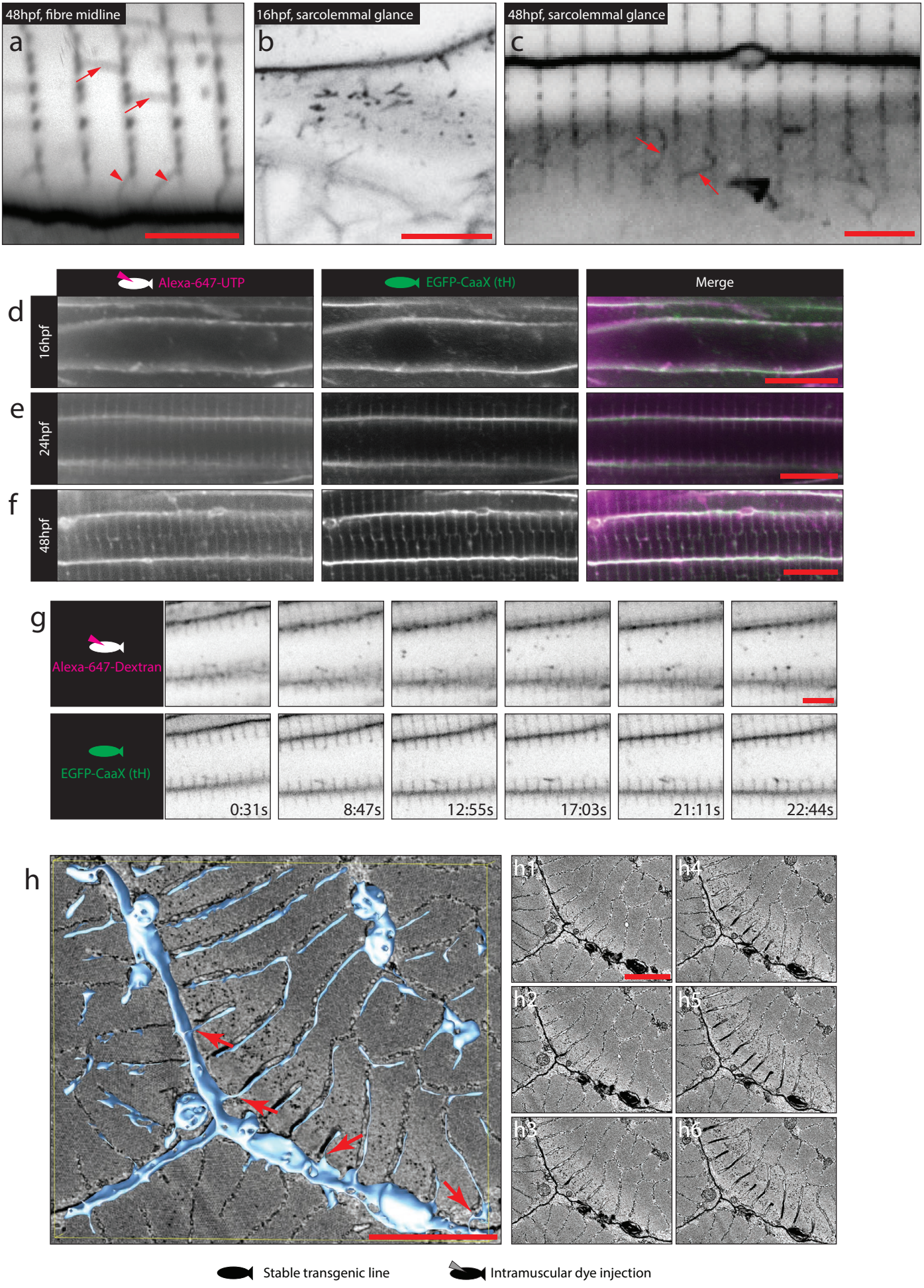
48hpf, fibre midline
a
16hpf, sarcolemmal glance
b
48hpf, sarcolemmal glance
c
Alexa-647-UTP
EGFP-CaaX (tH)
Merge
d
16hpf
e
24hpf
f
48hpf
g
Alexa-647-Dextran
EGFP-CaaX (tH)
0:31s
8:47s
12:55s
17:03s
21:11s
22:44s
h
h1
h2
h3
h4
h5
h6
Stable transgenic line
Intramuscular dye injection

Supplementary Figure 5, related to Figure 5

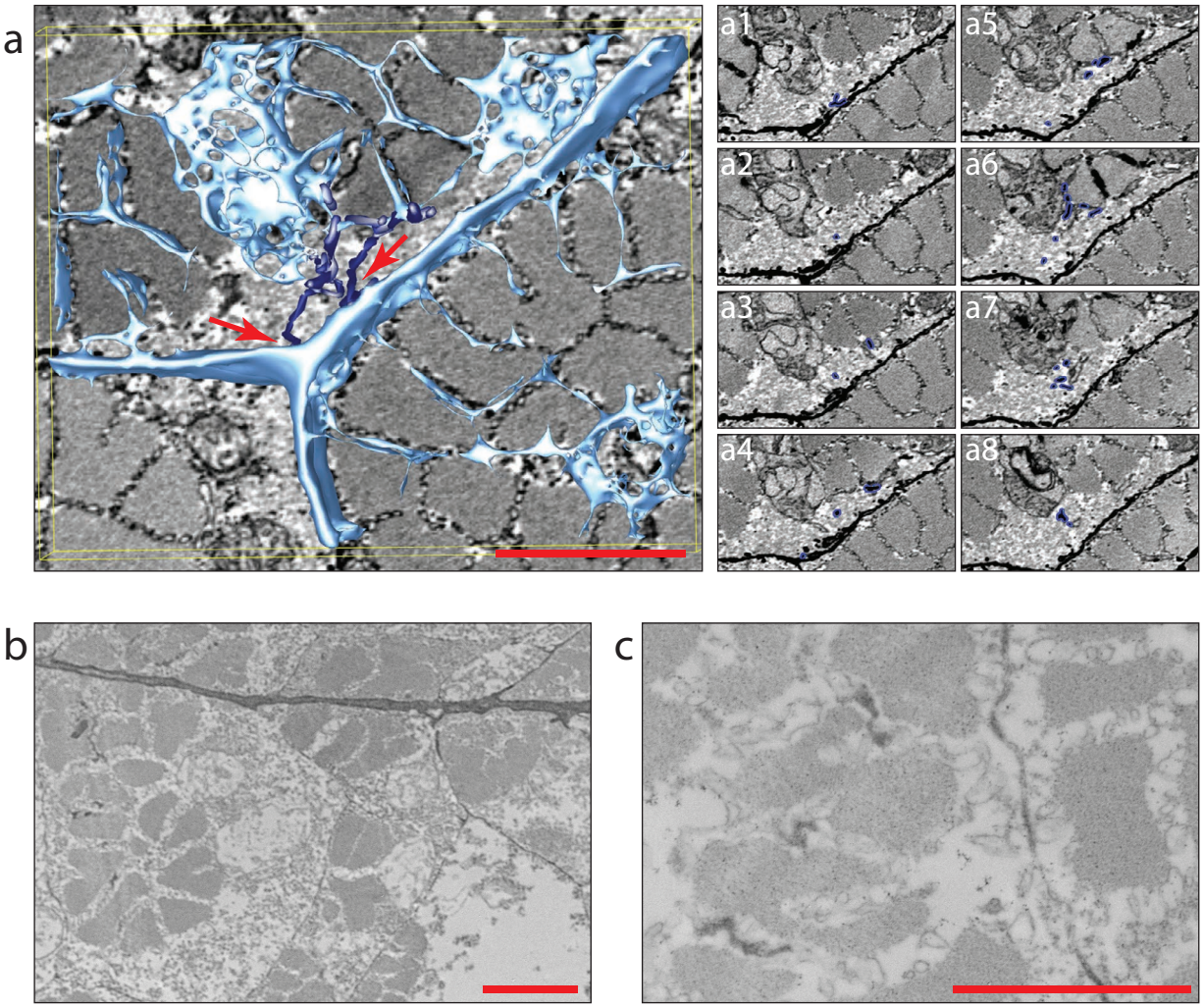

Figure 6

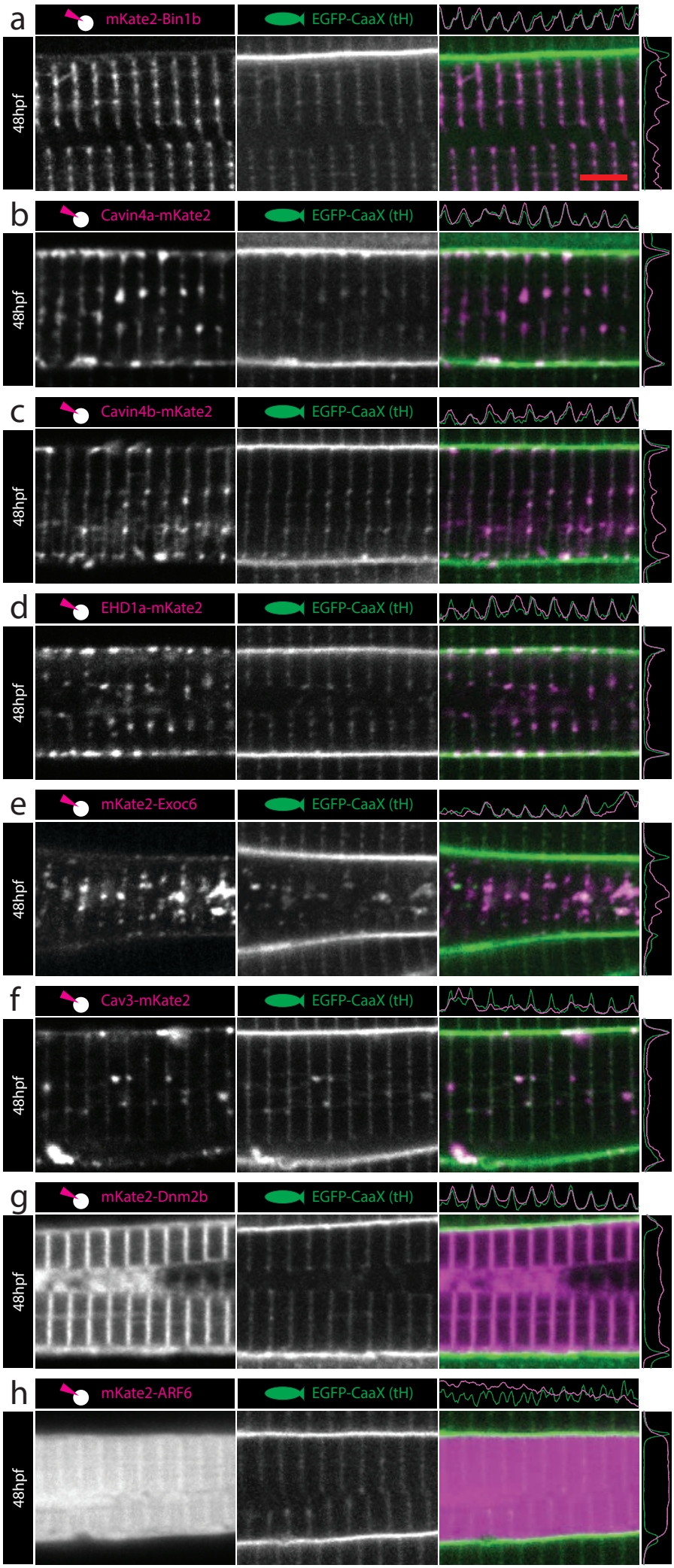

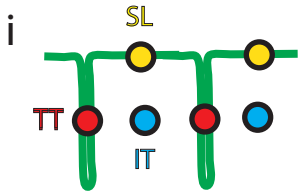

j

	CAAX SL	CAAX TT	CAAX IT	MARKER SL	MARKER TT	MARKER IT	Ratio TT:IT	
Bin1b	68	20	12	29	54	16	3.28	****
Cavin4a	73	17	10	53	34	13	2.62	***
Cavin4b	73	18	9	35	46	19	2.41	****
EHD1a	74	17	9	55	31	14	2.31	****
Exoc6 (Sec15)	73	16	11	32	46	22	2.11	****
Caveolin3	69	18	13	47	35	19	1.82	***
Dynamin2b	70	19	11	34	43	24	1.81	****
CD44b	77	15	8	60	26	15	1.74	**
Dysferlin	76	15	9	67	21	12	1.66	**
EHD1b	62	23	15	54	28	18	1.6	***
CaveolinY	55	25	20	52	30	19	1.59	**
EHD2b	70	17	13	38	38	24	1.59	***
Myotubularin	76	16	8	55	27	18	1.54	****
Pacsin2	75	16	9	76	14	10	1.47	***
CDC42	61	22	17	58	25	17	1.45	**
Clathrin LC b	70	19	12	60	23	17	1.34	**
Exoc7 (Exo70)	63	21	16	43	32	25	1.31	****
Bin1a	72	18	10	43	32	25	1.24	
Dynamin2a	70	18	11	46	29	25	1.15	
EHD2a	78	13	9	74	14	12	1.12	
ARF1	66	21	13	27	38	35	1.1	**
Clathrin LC a	69	19	12	37	33	30	1.08	
ARF6	69	18	13	25	38	37	1.04	
Exoc1 (Sec3)	69	19	12	37	31	32	0.96	

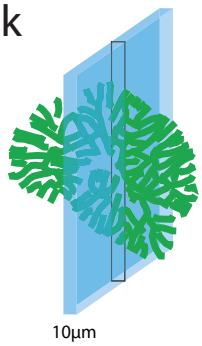

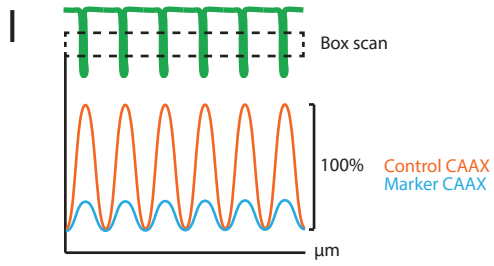

m

	localization	perturbation	% (of WT)
EHD1b	***	**	134
EHD1b-dEH	*		65
EHD1a	****	*	124
EHD1a-dEH	**		88
Dynamin2b	****		105
Dynamin2b-DN	**		83
Dynamin2a			91
Dynamin2a-DN	*		70
ARF6			94
ARF6-DN			114
ARF1	**		94
ARF1-DN	**		105
CDC42	**		91
CDC42-DN			85

+50%
-50%

Mosaic expression from DNA injection

Stable transgenic line

Supplementary Figure 6 related to Figure 6

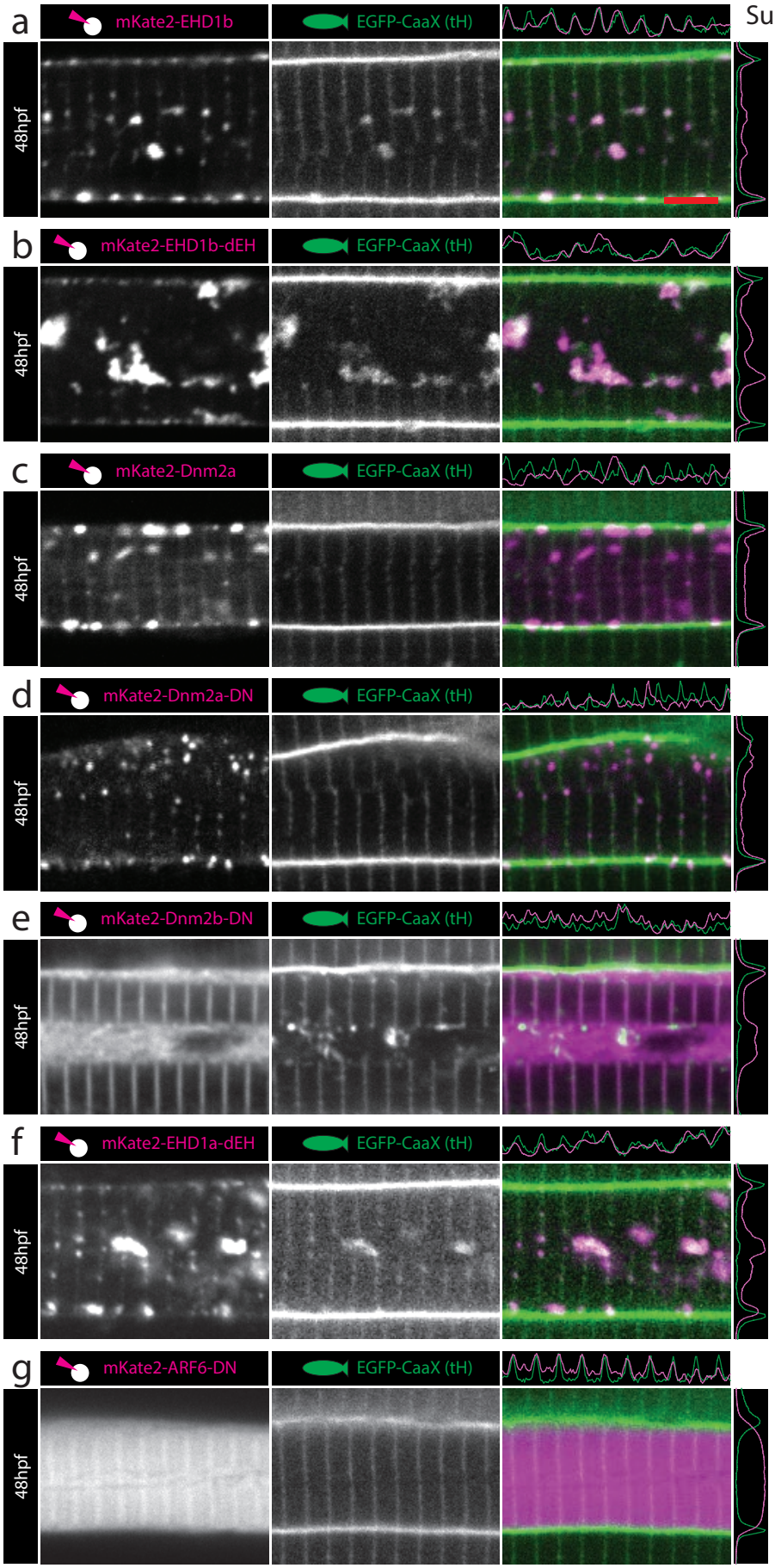

Mosaic expression from DNA injection

Stable transgenic line

Figure 7

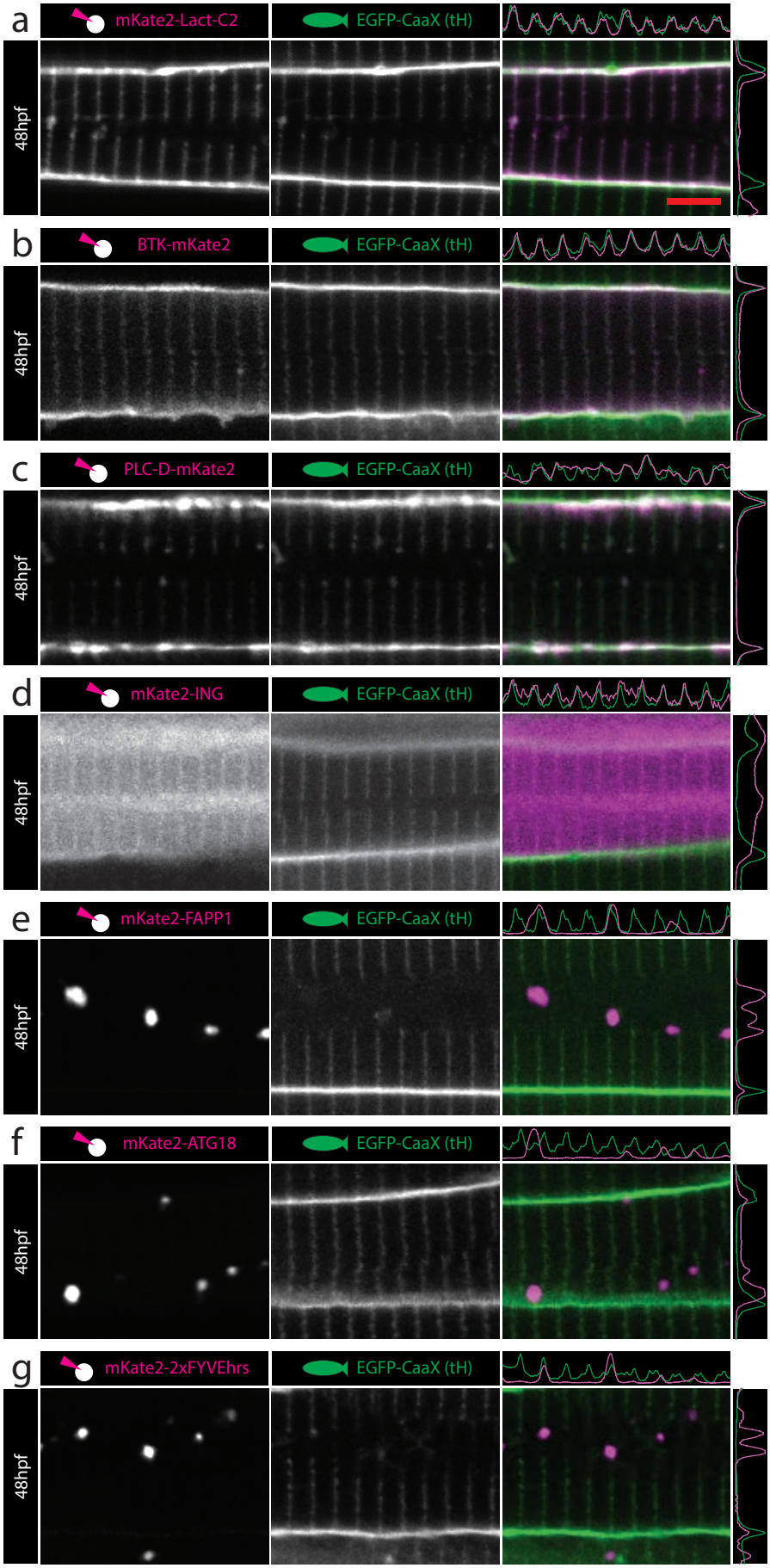

h

	CAAX			MARKER			Ratio	
	SL	TT	IT	SL	TT	IT	TT : IT	
LactC2 (PS)	66	20	15	62	25	13	1.92	****
BTK (PtdIns[3,4,5]P_3)	71	18	11	64	21	14	1.5	**
PLC-D (PtdIns[4,5]P_2)	70	17	12	66	20	14	1.43	*
INGdomain (PtsIns[5]P)	72	18	10	33	36	32	1.13	**
FAPP1 (PtsIns[4]P)	69	18	13	51	25	24	1.04	

Mosaic expression from DNA injection

Stable transgenic line

Supplementary Figure 7, related to Figure 7

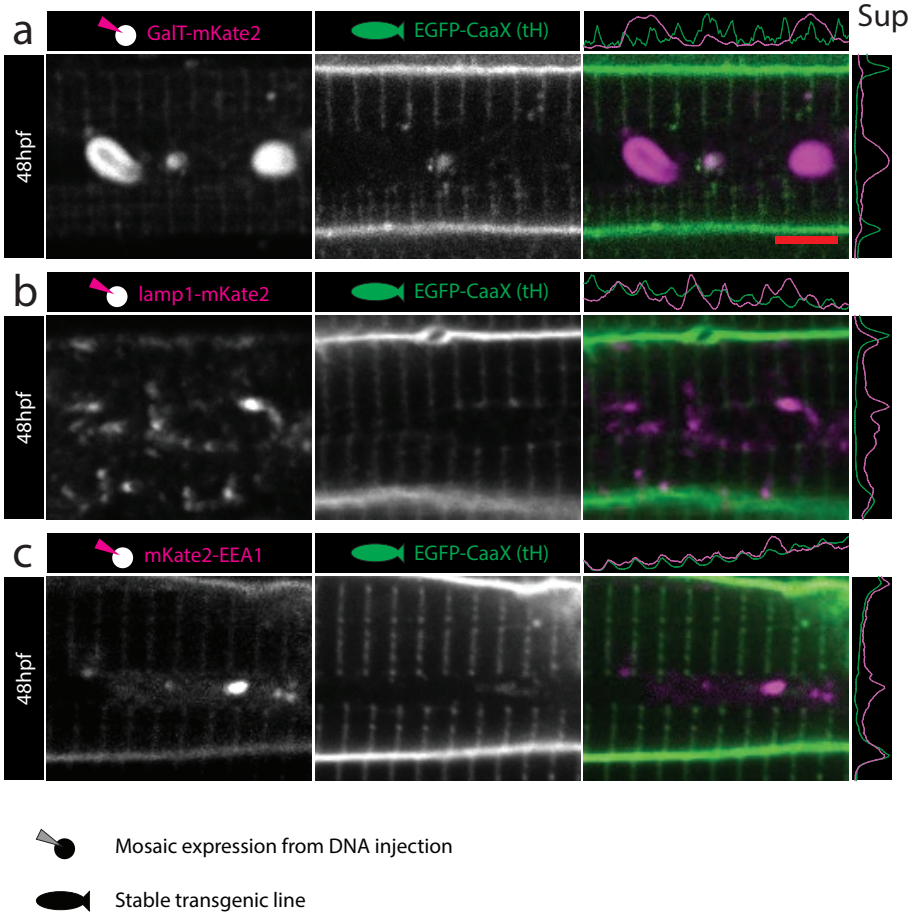

Figure 8

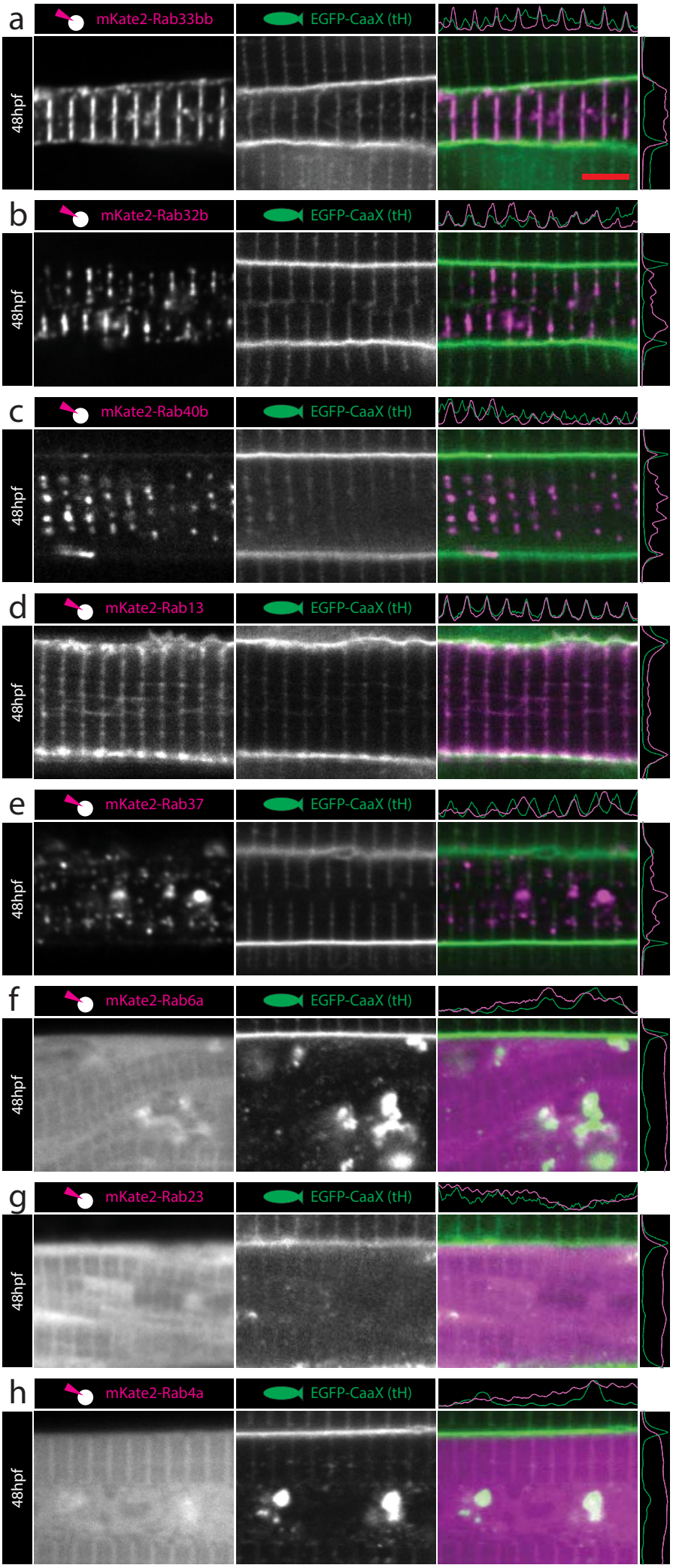
a
mKate2-Rab33bb
EGFP-CaaX (tH)
48hpf
b
mKate2-Rab32b
EGFP-CaaX (tH)
48hpf
c
mKate2-Rab40b
EGFP-CaaX (tH)
48hpf
d
mKate2-Rab13
EGFP-CaaX (tH)
48hpf
e
mKate2-Rab37
EGFP-CaaX (tH)
48hpf
f
mKate2-Rab6a
EGFP-CaaX (tH)
48hpf
g
mKate2-Rab23
EGFP-CaaX (tH)
48hpf
h
mKate2-Rab4a
EGFP-CaaX (tH)
48hpf

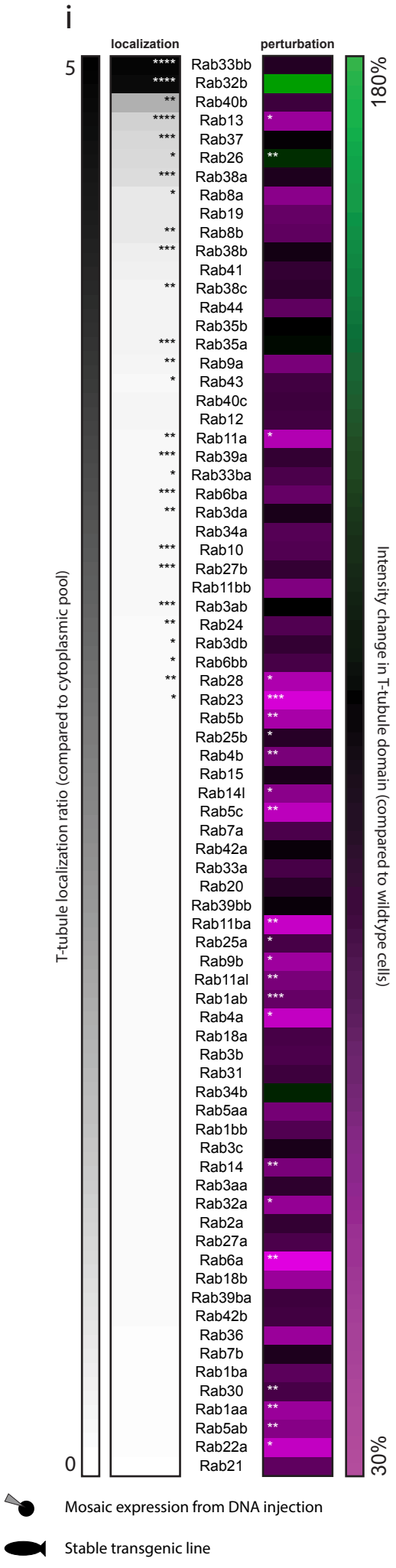
i
localization
perturbation
5
0
T-tubule localization ratio (compared to cytoplasmic pool)
Intensity change in T-tubule domain (compared to wildtype cells)
180%
30%
Rab33bb
Rab32b
Rab40b
Rab13
Rab37
Rab26
Rab38a
Rab8a
Rab19
Rab8b
Rab38b
Rab41
Rab38c
Rab44
Rab35b
Rab35a
Rab9a
Rab43
Rab40c
Rab12
Rab11a
Rab39a
Rab33ba
Rab6ba
Rab3da
Rab34a
Rab10
Rab27b
Rab11bb
Rab3ab
Rab24
Rab3db
Rab6bb
Rab28
Rab23
Rab5b
Rab25b
Rab4b
Rab15
Rab14l
Rab5c
Rab7a
Rab42a
Rab33a
Rab20
Rab39bb
Rab11ba
Rab25a
Rab9b
Rab11al
Rab1ab
Rab4a
Rab18a
Rab3b
Rab31
Rab34b
Rab5aa
Rab1bb
Rab3c
Rab14
Rab3aa
Rab32a
Rab2a
Rab27a
Rab6a
Rab18b
Rab39ba
Rab42b
Rab36
Rab7b
Rab1ba
Rab30
Rab1aa
Rab5ab
Rab22a
Rab21
Mosaic expression from DNA injection
Stable transgenic line

Supplementary Figure 8,
related to Figure 8

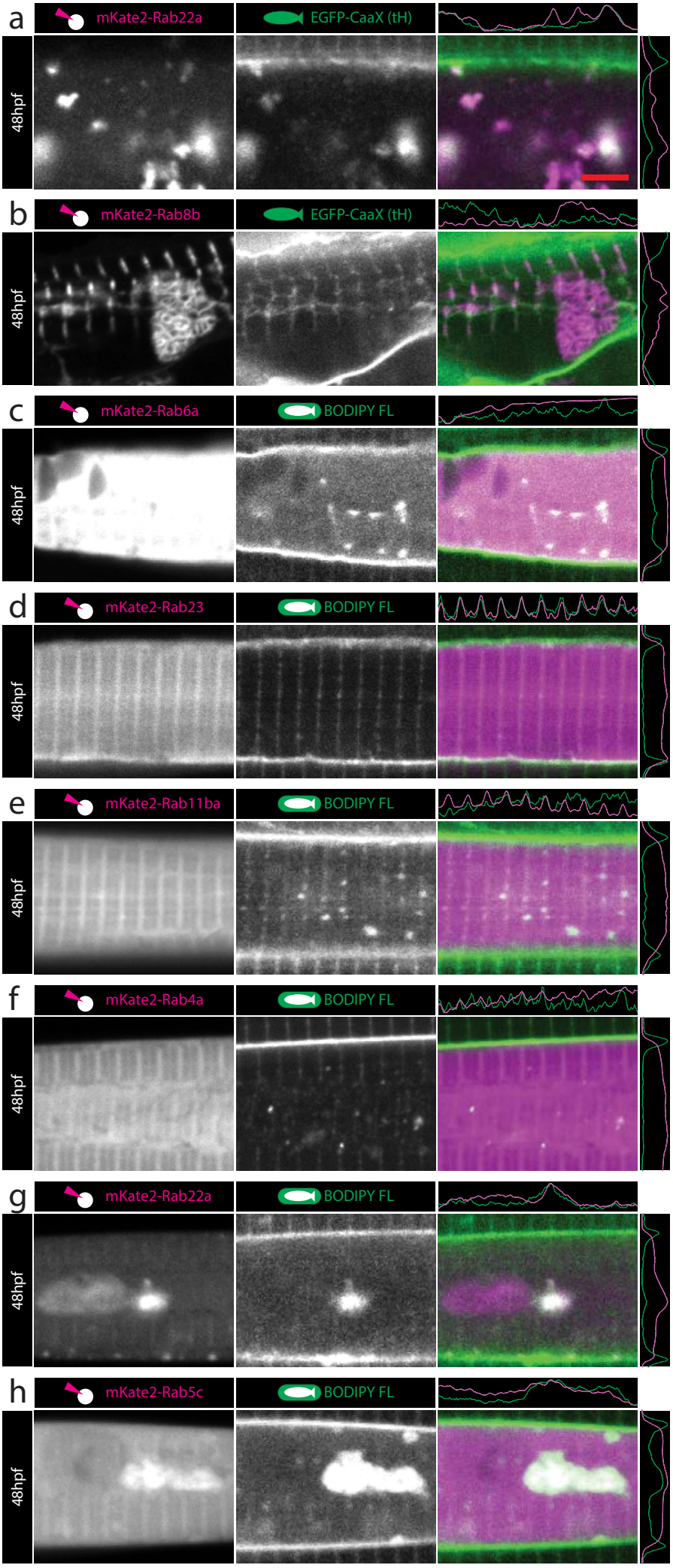

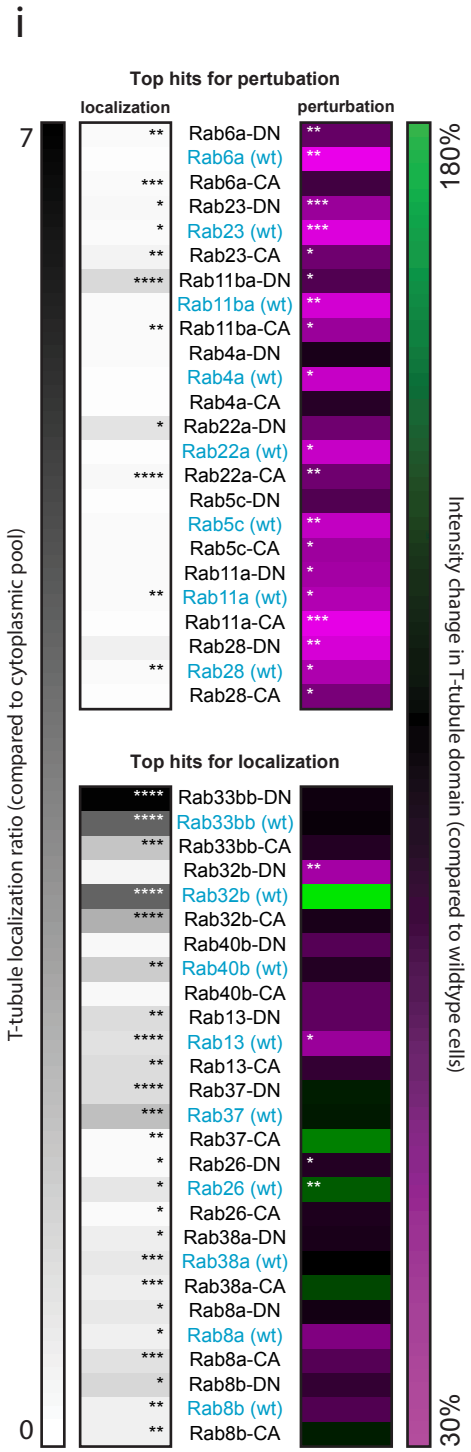

Mosaic expression from DNA injection

Stable transgenic line

Figure 9

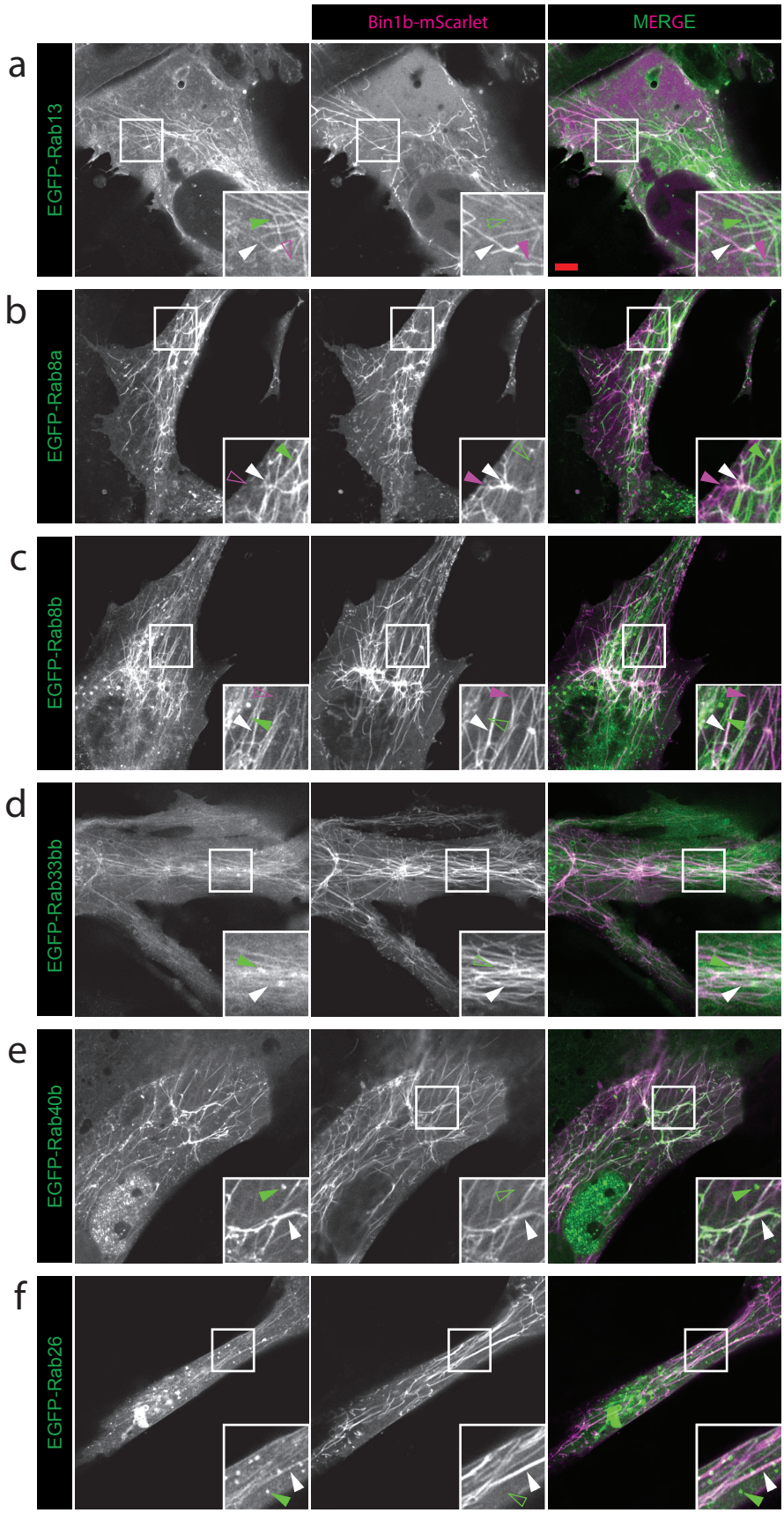
Bin1b-mScarlet
MERGE
a
EGFP-Rab13
b
EGFP-Rab8a
c
EGFP-Rab8b
d
EGFP-Rab33bb
e
EGFP-Rab40b
f
EGFP-Rab26

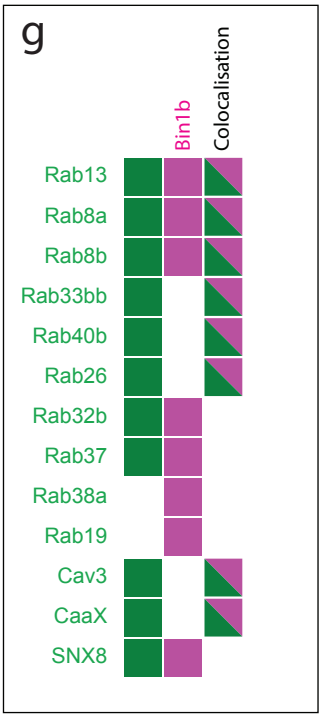
g
Bin1b
Colocalisation
Rab13
Rab8a
Rab8b
Rab33bb
Rab40b
Rab26
Rab32b
Rab37
Rab38a
Rab19
Cav3
CaaX
SNX8
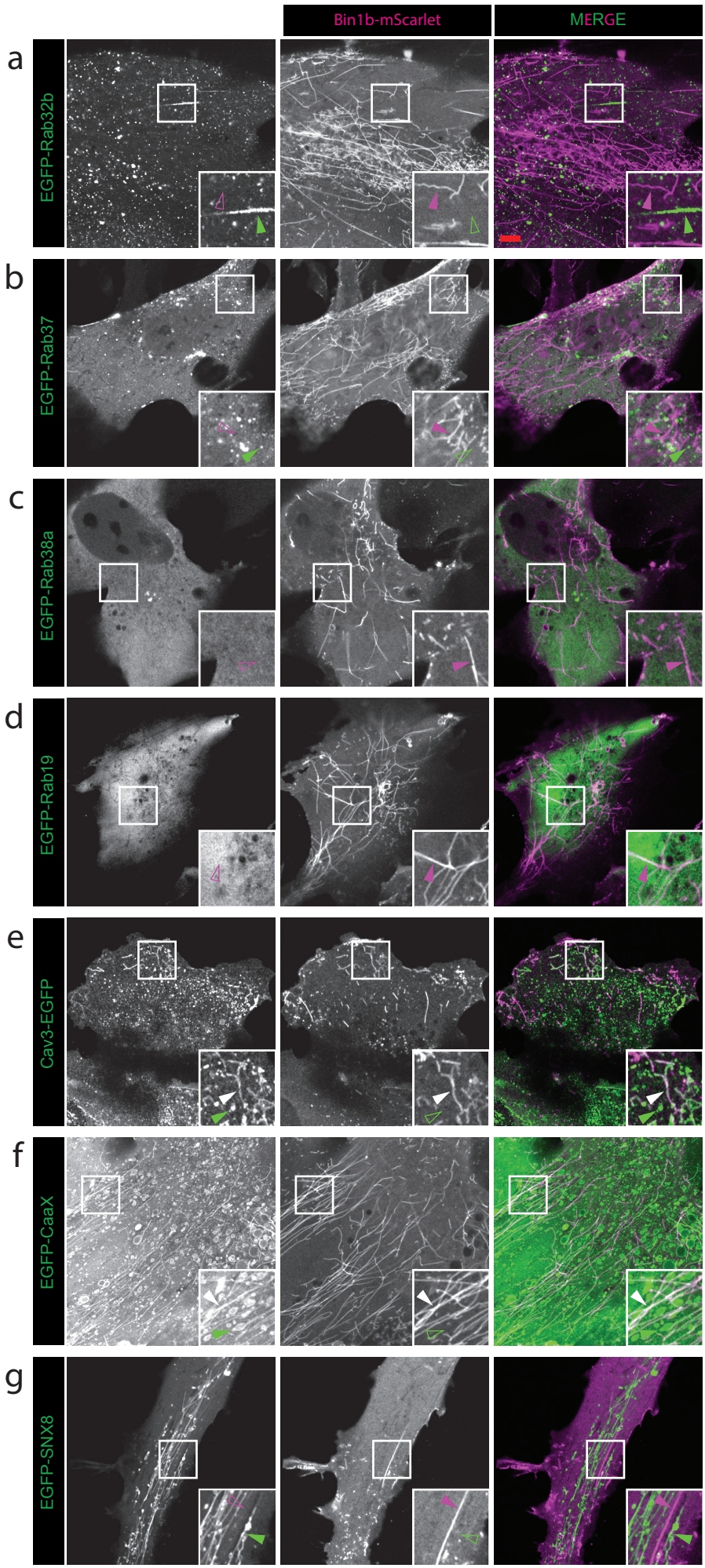
Supplementary Figure 9
related to Figure 9